PHOTOCHEMISTRY OF POLYCYCLIC AROMATIC HYDROCARBONS IN COSMIC WATER ICE: THE ROLE OF PAH IONIZATION AND CONCENTRATION

Amanda M. Cook[1], Alessandra Ricca[2], Andrew L. Mattioda[1], Jordy Bouwman[3], Joseph Roser[1],
Harold Linnartz[4], Jonathan Bregman[1], and Louis J. Allamandola[2]
[1] NASA Ames Research Center, PO Box 1, M/S 245–6, Moffett Field, CA 94035, USA
[2] SETI Institute, 189 North Bernardo Avenue, Mountain View, CA 94043, USA
[3] Radboud University Nijmegen, Institute for Molecules and Materials, Toernooiveld 5, 6525 ED Nijmegen, The Netherlands
[4] Sackler Laboratory for Astrophysics, Leiden Observatory, University of Leiden, PO Box 9513, NL2300 RA Leiden, The Netherlands

ABSTRACT

Infrared spectroscopic studies of ultraviolet (UV) irradiated, water-rich, cosmic ice analogs containing small polycyclic aromatic hydrocarbons (PAHs) are described. The irradiation studies of anthracene:H_2O, pyrene:H_2O, and benzo[ghi]perylene:H_2O ices (14 K) at various concentrations reported by Bouwman et al. are extended. While aromatic alcohols and ketones have been reported in residues *after* irradiated PAH:H_2O ices were warmed to 270 K, it was not known if they formed during ice irradiation or during warm-up when reactants interact as H_2O sublimes. Recent work has shown that they form in low temperature ice. Using DFT computed IR spectra to identify photoproducts and PAH cations, we tentatively identify the production of specific alcohols [PAH(OH)$_n$] and quinones [PAH(O)$_n$] for all PAH:H_2O ices considered here. Little evidence is found for hydrogenation at 14 K, consistent with the findings of Gudipati & Yang. Addition of O and OH to the parent PAH is the dominant photochemical reaction, but PAH erosion to smaller PAHs (producing CO_2 and H_2CO) is also important. DFT spectra are used to assess the contribution of PAH-related species to interstellar absorption features from 5 to 9 μm. The case is made that PAH cations are important contributors to the C2 component and PAH(OH)$_n$ and PAH(O)$_n$ to the C5 component described by Boogert et al. Thus, interstellar ices should contain neutral and ionized PAHs, alcohols, ketones and quinones at the ∼2%–4% level relative to H_2O. PAHs, their photoproducts, and ion-mediated processes should therefore be considered when modeling interstellar ice processes.

Key words: astrochemistry – ISM: abundances – ISM: clouds – ISM: molecules – molecular data – molecular processes

1. INTRODUCTION

Infrared (IR) astronomical observations indicate that photon-dominated regions (PDRs) contain large abundances of polycyclic aromatic hydrocarbons (PAHs), as evidenced by strong gas-phase PAH emission (Peeters et al. 2004; van Dishoeck 2004; Tielens 2008, and references therein). However, PAH emission is suppressed and ultimately extinguished moving into denser regions of the ISM where gas-phase species like PAHs condense onto very cold grains ($T \leqslant 30$ K), largely as neutral PAHs frozen in H_2O-rich mantles. IR absorption features detected at 3.3 μm (Smith et al. 1989; Sellgren et al. 1995; Brooke et al. 1999), 6.2 μm (Chiar et al. 2000; Keane et al. 2001), and 11.3 μm (Bregman et al. 2000) in the spectra of a limited number of young stellar objects (YSOs) have been attributed to PAHs. Hardegree-Ullman et al. (2014) suggest that frozen neutral PAHs account for 2%–9% of the unidentified absorption in the 5–8 μm spectral region of YSOs.

Furthermore, the ice mantles frozen out onto the dust grains in dense clouds are subjected to irradiation by the attenuated UV photon field as well as cosmic ray impacts (e.g., Garozzo et al. 2011; Chang & Herbst 2014). These sources of energy can drive chemistry within the ice mantles by breaking molecular bonds, ionizing adsorbed molecules, or by locally heating the ice mantle. If these dust grains subsequently diffuse into regions with strong UV radiation fields, the ice mantles will be sublimated and contribute a chemically enriched population of molecules to the gas-phase chemistry. It is expected that PAHs and PAH-derived molecules also play a role in this enriched gas-phase chemistry.

Laboratory studies have been performed to measure the IR spectra of neutral PAHs in water ices (Sandford et al. 2004; Bernstein et al. 2005a, 2005b) and of PAH cations in solid H_2O (Bernstein et al. 2007) with the goal of helping in the detection of PAHs in dense interstellar clouds. Due to the presence of very strong H_2O ice bands overwhelming the much weaker PAH IR features, laboratory experiments typically use PAH:H_2O concentrations that are higher than 1:50, which is estimated to be the PAH concentration in astrophysical ices (Bouwman et al. 2011b). Optical spectroscopy, which avoids this band blending, has successfully overcome this limitation. Together, these IR and optical studies have shown that PAHs in water ices subjected to UV irradiation can undergo ionization and photochemical reactions to produce oxidized aromatic compounds (Bernstein et al. 1999, 2003; Gudipati 2004; Gudipati & Allamandola 2006; Ashbourn et al. 2007; Guennoun et al. 2011a, 2011b; Bouwman et al. 2011b; Keheyan & ten Kate 2012). Computationally, Ricca & Bauschlicher (2000) have shown that the addition of the OH radical to neutral naphthalene and the naphthalene cation is barrierless.

Utilizing the optical technique, Cuylle et al. (2014) recently examined the effects of PAH concentration (relative to H_2O) on ionization efficiency. The ionization efficiency drops from over 60% at very low concentrations (1:10,000) to 15% at higher concentrations (1:1000). An earlier mid-IR study of UV photolyzed PAH:H_2O ices (PAH = anthracene, pyrene, and

benzo[ghi]perylene) showed that the production of PAH photoproducts is also dependent on PAH concentration (Bouwman et al. 2011b).

The present work extends the Bouwman et al. (2011b) study by characterizing the types of photoproducts formed by comparing experimental spectra with DFT computed spectra. In addition, this work also quantifies the concentration dependence of two main aspects of PAH reactivity in H_2O ice: the formation of aromatic photoproducts that do not degrade the parent PAH, *and* PAH erosion to form CO_2 and H_2CO. We primarily focus upon varying the concentration of anthracene in water ice for UV irradiation studies and use similar UV irradiation of pyrene and benzo[ghi]preylene in water ice at high concentration as comparison experiments.

This extensive study, which includes theoretically calculated spectra of predicted photoproducts, quantifies the most important factors for the evolution of PAHs in astrophysical ices: ionization, oxygenation, hydroxylation, and erosion to smaller PAHs and stable end products. The laboratory and theoretical spectra presented here provide deep insight to the interpretation of IR absorption bands observed in the dense interstellar medium (Gibb & Whittet 2002; Boogert et al. 2008), particularly from 5–9 μm.

2. EXPERIMENTAL TECHNIQUE AND THEORETICAL METHODS

2.1. Laboratory Methods

The experimental techniques used for this study have been described elsewhere (Hudgins et al. 1994; Bouwman et al. 2011b). Here we describe the details relevant for this particular work. Samples were prepared by vapor co-deposition of H_2O and a single PAH species onto a cryogenically cooled, IR-transparent CsI window suspended in vacuum ($P \leqslant 10^{-8}$ Torr) with the window temperature held at 15 K throughout the experiment. Water vapor is Milli-Q grade filtered, deionized water with contaminant gases removed by three freeze–pump–thaw cycles. PAH vapor was thermally sublimated from a sample kept within a pyrex tube hermetically sealed to the vacuum chamber. To prepare different levels of PAH:H_2O concentrations, the PAH deposition temperature was varied between experiments, while the H_2O flow remained constant.

The column density of H_2O deposited onto the window in each experiment was calculated as in Bouwman et al. (2011b), using H_2O band strength values from Hudgins et al. (1993). Three different PAH molecules are considered here, namely anthracene ("Anth" $C_{14}H_{10}$, Aldrich, 100%), pyrene ("Py", $C_{16}H_{10}$, Aldrich, 99%), and benzo[ghi]perylene ("$B_{ghi}P$", $C_{22}H_{12}$, Aldrich, 98%). Their structures are shown in Figure 1, labeled a1, p1 and b1, respectively. The PAH column density is determined using the average of four or five of the strongest PAH bands for each PAH and the absolute band intensities calculated by Bouwman et al. (2011b).

Once ice deposition was complete, the mid-IR spectrum of the neutral (i.e., un-photolyzed) PAH:ice sample was measured for each sample. Next, each ice sample was photolyzed with UV radiation from a flowing-H_2, microwave discharge lamp. The reported radiation spectrum from this type of lamp includes Lyα (121.6 nm) and a complex of molecular H_2 lines centered at 160 nm; we assume a total UV photon flux of $\sim 10^{15}$ photons cm^{-2} s^{-1} at the ice surface based on measurements of analogous lamp models and parameters (Warneck 1962; Allamandola et al. 1988; Cook et al. 2014).

A BioRad Excalibur FTS 4000 FTIR spectrometer with a KBr beamsplitter and a liquid-N_2 cooled MCT detector was used to measure absorption spectra, in transmission, of the deposited ices. Each spectrum reported here represents 512 co-added spectral scans recorded at 0.5 cm^{-1} resolution. Background spectra were collected just before ice deposition. Additional spectra were recorded after 0, 5, 10, 15, 30, 60, 120, and (usually) 180 minutes of cumulative UV exposure of the newly deposited ice layer.

2.2. Continuum Determination and Baseline Correction

Integration of PAH bands requires careful attention to continuum determination, particularly since our continua are dominated by strong H_2O bands.

The underlying continuum is typically smooth for neutral ices with PAH bands in the 1650–1000 cm^{-1} region and can be approximated with a spline fit to regions with no absorption bands. However, some of the weaker photoproducts can be difficult to pick out of the continuum once the ices are photolyzed. It is much easier to discern photoproduct bands when a spectrum of the neutral species is subtracted from the photolyzed spectrum. It is possible, in principle, to subtract a multiplicative factor of a given neutral spectrum from a photolyzed spectrum, fine tuning the subtraction factor so that all neutral species are perfectly removed. However, we note that this fine-tuning often results in a difficult comparison of the spectra as different photolysis times are investigated for a given experiment; sometimes it is unclear whether weakly observed features (particularly those that appear near strong neutral bands) are the result of varying subtraction factors, or whether they are real photoproduct bands growing in. Therefore, to remove this confusion, the subtraction factor of one was used for all of our neutral-subtracted spectra.

Once neutral spectra are subtracted from photolyzed spectra, the positive bands should be the result of photoproducts. However, both the narrow individual bands and the broad water bands that form the underlying continuum are affected by photolysis. The region around 1600 cm^{-1} requires special attention because the H–O–H bending mode of water shifts to higher frequencies upon photolysis. Consequently, subtracting the neutral spectrum from the photolyzed spectrum introduces some artifacts. For this reason, many of the neutral-subtracted spectra presented in this paper are not baseline-corrected in the region from 1640 to 1500 cm^{-1}. By skipping the baseline correction for this region, we can more easily identify oversubtraction artifacts and baseline shifting artifacts. Baseline correction is generally possible for neutral-subtracted spectra at frequencies below 1500 cm^{-1}, as reflected in our figures.

2.3. Theoretical Methods

2.3.1. Computed PAH IR Spectra

The structures for each of the three PAHs studied here were fully optimized by finding the three-dimensional arrangement of the atoms that minimizes the total energy and the harmonic frequencies computed using density functional theory (DFT). We used the hybrid B3LYP functional (Becke 1993; Stephens et al. 1994) in conjunction with the 6–31G* basis set of Frisch et al. (1984). The computed B3LYP/6–31G* harmonic frequencies were scaled to lower frequencies using two scale factors, namely 0.972 for non-C–H stretches and 0.96 for C–H stretches, as required for agreement with the measured experimental fundamental frequencies of PAH molecules isolated in argon matrices (Bauschlicher & Ricca 2010).
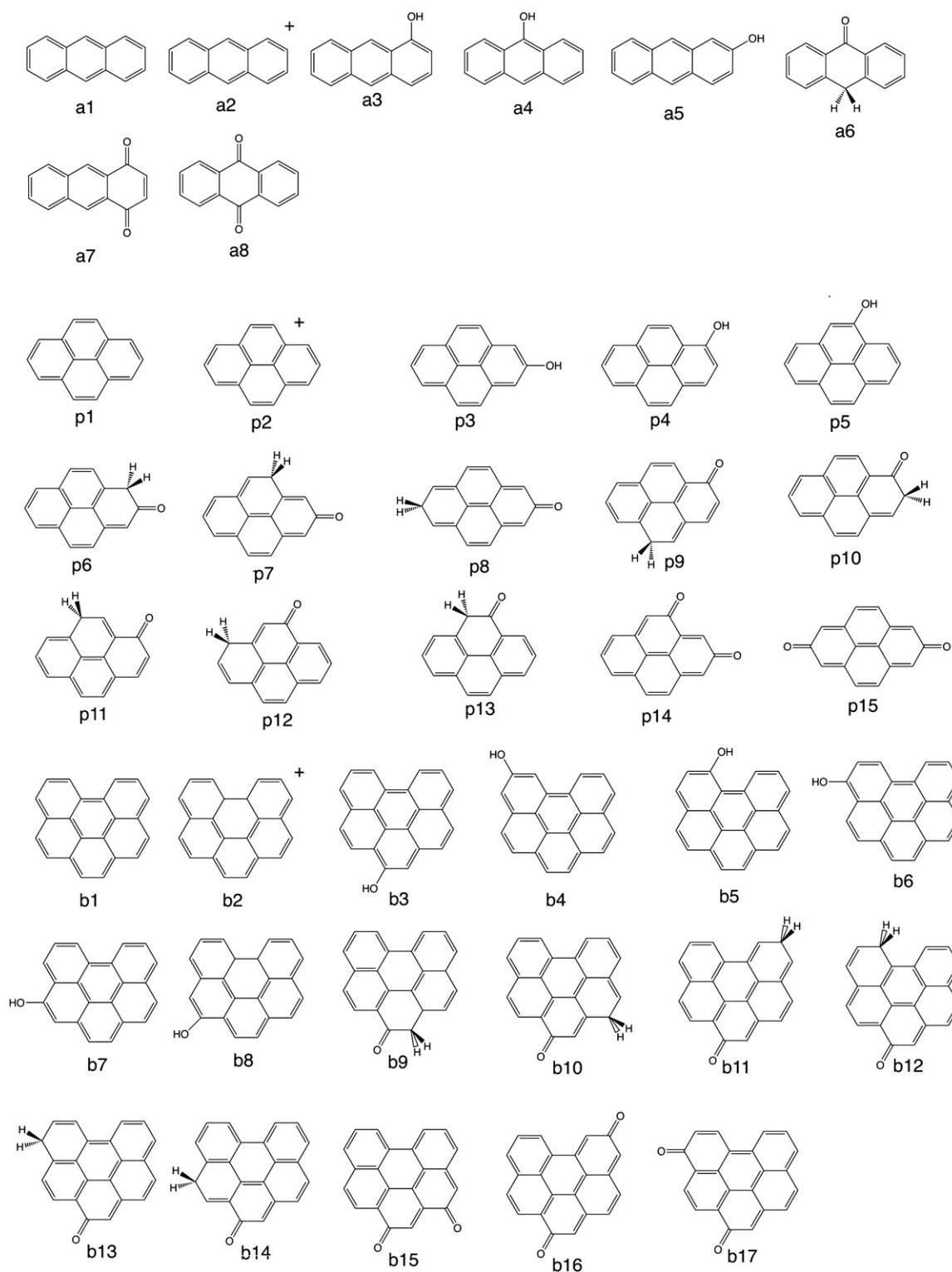
Figure 1. Structures of the PAHs and PAH-related species computationally considered here: anthracene ("a"), pyrene ("p"), and benzo[ghi]perylene ("b"), their cations, and predicted UV photoproducts due to OH- and O-substitution. Corresponding calculated spectra are shown in Figure 3.

The positions of the non-C–H stretching vibrational modes computed using the 6–31G* basis set have an average absolute error of 7.1 cm^{-1} and a maximum absolute error of 22.4 cm^{-1}. The positions of the C–H stretching vibrational modes have an average absolute error of 2.5 cm^{-1} and a maximum absolute error of 5 cm^{-1} (Bauschlicher & Ricca 2010). The ketone stretching frequencies (ν_{C-O}) have larger errors than the other functional groups and need to be scaled by 0.952 to match experiment. To aid visual comparison with the experimental spectra, we broadened our computed results with a 5 cm^{-1} FWHM, Gaussian profile for all bands.

All calculations were performed using the Gaussian 09 program (Frisch et al. 2009) and the interactive molecular

3

graphics tool MOLEKEL (Flükiger et al. 2000) was used to aid the analysis of the vibrational modes.

2.3.2. Computed PAH Monomer and Aggregate Fractions

The monomer fraction has been estimated using the model described in Roser et al. (2014), in which each PAH molecule is modeled as the union of sphere-swept disks, one for each ring in the aromatic structure. Numerical results are developed in three steps. First, trial molecules are randomly distributed throughout a cubic trial space with each molecule given a random orientation. Second, a procedure to resolve overlapped molecules is applied. Finally, the volume fraction occupied by the surviving PAH molecules and the monomer fraction (i.e. the number of surviving molecules with no nearest neighbor within a cut-off distance of 5 Å) is computed using only the interior volume of original trial space to avoid edge effects. To connect experimental results to the model output, we assume that the volume fraction occupied by PAH molecules is simply proportional to the PAH:H_2O column density ratio by a factor of 6.45 for anthracene, 7.15 for pyrene, and 9.50 for benzo[ghi]perylene. The monomer fraction for the experimental matrix deposits is then determined by fitting an exponential curve to the computed monomer fraction as a function of one minus the filled volume fraction and then interpolating. Applying this model (Roser et al. 2014) shows that the monomer fraction for anthracene is approximately: 67% for PAH:H_2O = 1:770, 59% for 1:590, 28% for 1:260, 0.4% for 1:80 and 0% for 1:20. The monomer fraction for pyrene is approximately 4% for 1:110, 1% for 1:90 and 0% for 1:70. For benzo[ghi]perylene, the monomer fraction is 28% for 1:310, 5% for 1:150, and 0% for 1:70. These results indicate PAH monomers will be important at low PAH concentrations. Conversely, PAH clusters become very important at high PAH concentrations.

3. RESULTS

3.1. Theoretically Calculated IR Spectra of PAH Photoproducts

As will be shown below, the principle PAH-related photoproducts initially formed include PAH cations, alcohols, and ketones. After first generating PAH cations, UV photolysis of PAHs in water ice is expected to produce aromatic alcohols as the first chemical photoproducts within the ice; with increasing photolysis time, these aromatic alcohols are then expected to transform into ketones (Gudipati 2004; Gudipati & Allamandola 2006; Ashbourn et al. 2007; Guennnon et al. 2011a, 2011b; Gudipati & Yang 2012; Yang & Gudipati 2014). For example, the UV irradiation of phenol, the simplest aromatic alcohol, induces the breaking of the O−H bond to form a phenoxyl radical (Giuliano et al. 2012); see Figure 2. If hydrogen atoms are present, as expected from the UV-irradiated H_2O as well as the other phenols in the ice, they can recombine with the phenoxyl radical to form either the phenol or a ketone (Guennoun et al. 2011a, 2011b). From this step, two ketone isomers can then form, namely 2,4- or 2,5-cyclohexadienone. Decomposition of the ketone occurs via the 2,4-cyclohexadienone isomer, which is a photochemically unstable α-ketone and undergoes a ring opening to form a ketene. Ketenes are unstable and can then further decompose either by losing a CO molecule (Dauben et al. 1975; Giuliano et al. 2012) or form an alcohol.

Spectroscopically, aromatic alcohols have three main characteristic modes in the 1400–1000 cm^{-1} region as exemplified by phenol, the simplest of the aromatic alcohols (Michalska et al. 1996; Giuliano et al. 2012). First, the O−H in-plane bending
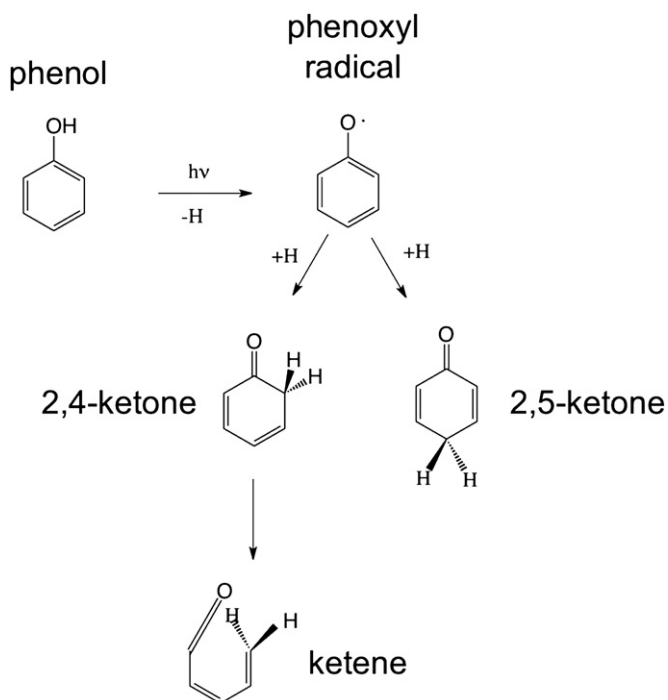

Figure 2. Schematic showing the decomposition of phenol, the simplest aromatic alcohol, upon UV photolysis (see Section 3.1).

mode (δ_{O-H}, near 8.3 μm) usually has a strong intensity. It couples with the skeletal C−C stretching (ν_{C-C}) and the in-plane C−H bending (δ_{C-H}) modes to produce a second band denoted as $\nu_{C-C} + \delta_{C-H} + \delta_{O-H}$, which falls near 8 μm. Third, the X-sensitive mode (X_{sens}), where X represents the substituted group or atom, involves the motion of both the phenyl ring and the attached group; this mode falls near 7.6 μm.

PAH cations are also known to have much stronger bands in the 1650–1000 cm^{-1} range than their neutral counterparts (e.g., Allamandola et al. 1999, and references therein). Replacing an H atom on the periphery of a PAH with an electron-withdrawing substituent, such as OH or double bonded O, creates a positive charge localized on the attached carbon in the ring, but has little effect on the charge of the remaining carbon atoms. This has the effect of increasing the intensities of the modes involving the C−X bond.

To characterize the PAH photoproducts produced in our experiments we compute the IR spectra of several isomers of OH-substituted(alcohol) and CO-substituted (ketone)Anth, Py, and B$_{ghi}$P, which are shown in Figure 1 (structures) and Figure 3 (spectra). For simplicity, we denote Anth as "a", Py as "p", and B$_{ghi}$P as "b". Other mono-substituted ketones besides a6 have been computed for Anth (including the photochemically unstable α-ketones shown in Figure 2). However, these species only produced weak bands in the 1650–1000 cm^{-1} region and are not shown in Figure 3. In Figure 3, the spectra of neutral Anth (a1), Py (p1), and B$_{ghi}$P (b1) are multiplied by a factor of five or six since the neutral band intensities in the 1650–1000 cm^{-1} range are considerably smaller than the band intensities of cation structures a2, p2, and b2.

Our theoretical studies are focused on the 1650–1000 cm^{-1} spectral region, to compare with experimental data that does not suffer from overlap with the broad H_2O bands.

All of the mono-substituted alcohols shown in Figure 3 have their strongest bands in the 1350–1100 cm^{-1} region. The position of the δ_{O-H}, X_{sens} and $\nu_{C-C} + \delta_{C-H} + \delta_{O-H}$ bands
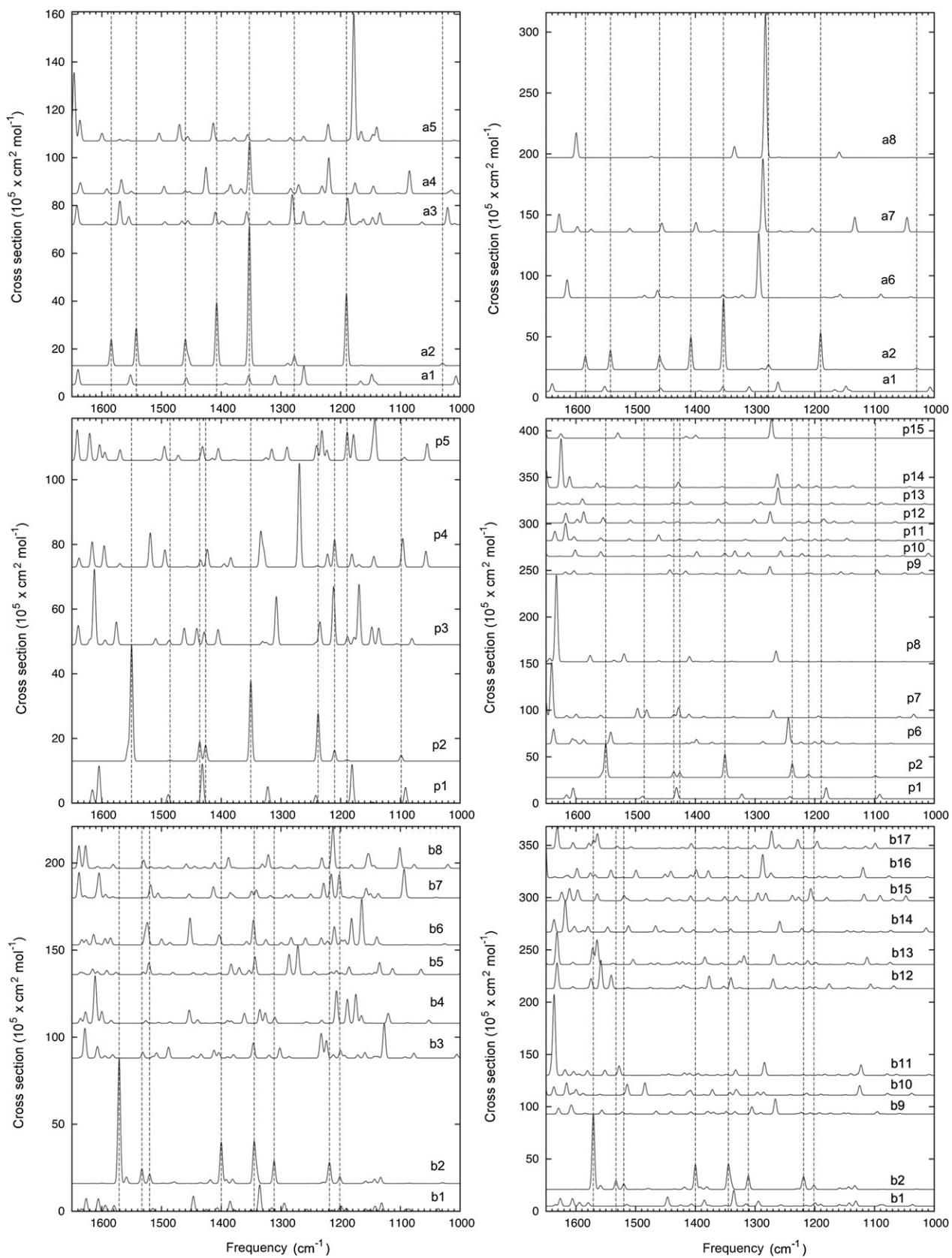
Figure 3. Theoretically calculated IR spectra for neutral and ionized Anth, Py, and B$_{ghi}$P, along with theoretical spectra of predicted photoproducts resulting from OH (alcohols)- and O-(ketones and quinones) substitution. See Figure 1 for the structures corresponding to the spectral identification a1, a2, . . . , a8, etc. Band frequencies > ~30 km mol^{-1} are listed in Tables 1–3.

Table 1
Anthracene Photoproduct Bands

Position (cm⁻¹) H₂O	Position (cm⁻¹) Argon[a]	I. A. in H₂O after 15 minutes of UV[b]	Theoretically Predicted Bands within ±/−20 cm⁻¹ of measured position in H₂O[c]	Band Strengths of Theoretical Bands (km/mol)	Possible Photoproduct Species (modes: δ, x, ν)
587	–	0.0011	–	–	–
649	–	0.0029	–	–	–
1157	–	0.0016	1140, 1159, 1159	31, 12, 12	a5, a8, a8
1178 (sh)	–	sh	1188, 1178 (OH)	283, 59	a3$^\delta$, a5$^\delta$
	1183.3	–	–	–	–
1190	1188.6	0.0109	1190 (+), 1188, 1178 (OH)	160, 283, 59	+, a3$^\delta$, a5δ
1292	1290.4	0.0008	1281 (OH), 1282, 1286, 1293 (CO)	67, 629, 320, 282	a3^x, a8, a7, a6
1326	1314.6	0.0054	1334 (CO)	48	a8
1340	1341	0.0104	1352 (+), 1352(OH), 1334 (CO)	311, 116, 48	+, a4$^\nu$, a8
1358 (sh)	1352.6	sh	1352 (+), 1352(OH), 1334 (CO)	311, 116, 48	+, a4$^\nu$, a8
	1364.4	–	–	–	–
1389	–	0.0003	1399 (CO)	41	a7
1394	–	0.0003	1399 (CO)	41	a7
1412	1406.1	0.004	1407 (+)	141	+
	1409.5	–	–	–	–
1419	1418.4	0.017	1413, 1426 (OH)	40, 58	a5, a4
1424 (sh)	1430.2	sh	1413, 1426 (OH)	40, 58	a5, a4
1459	–	0.0077	1460 (+), 1456 (CO)	57, 37	+, a7
1468	1456.5	0.0011	1469 (OH)	37	a5
1515	–	0.0032	–	–	H₂CO (CH₂ scissor mode)
1541	1539.9	0.0012	1542 (+)	84	+
1589	1586.4	0.0023	1584 (+)	58	+
1605	–	0.1402	1614, 1615 (CO)	32, 50	a6
1717	–	0.0003	1662 (CO), H₂CO	184, n/a	a6, H₂CO[d]
2136	–	0.0008	–	–	CO
2275	–	0.0003	–	–	
2341	–	0.0296	–	–	CO₂
2850	–	0.0231	–	–	H₂CO, other aliphatics

Notes. Theoretical spectra from 1650–1000 cm⁻¹ are shown in Figure 3. The abbreviation "sh" stands for shoulder. These bands are manifested as a shoulder on the side of another nearby band. The abbreviation I.A. stands for integrated absorbance.

[a] From Bouwman et al. (2011a). Columns with a "–" were not reported or sought in Bouwman et al. (2011a).

[b] The integrated absorbances (I.A.) reported here correspond to the Anth:H₂O = 1:590 mixture.

[c] Only predicted bands with band strengths >30 km mol⁻¹ are reported.

[d] CO stretch of H₂CO has a band strength of 9.6e-18 cm per molecule, from Schutte et al. (1996).

[δ] δ_{O-H} band.

[x] X_{sens} band.

[ν] $\nu_{C-C} + \delta_{C-H} + \delta_{O-H}$ band.

varies depending on the position of the substitution. The final columns of Tables 1–3 highlight these particular vibrational modes with "δ," "x", and "ν" superscripts, for the δ_{O-H}, X_{sens} and $\nu_{C-C} + \delta_{C-H} + \delta_{O-H}$ bands, respectively.

Overall, the δ_{O-H} and the X_{sens} modes are those with the strongest intensities. The δ_{O-H} bands occur between 1170 and 1230 cm⁻¹ for Anth and Py. For B$_{ghi}$P, which has more sites available for substitutions, the range in positions is greater, from 1130 to 1290 cm⁻¹. The X_{sens} bands usually fall between 1200 and 1350 cm⁻¹. The $\nu_{C-C} + \delta_{C-H} + \delta_{O-H}$ bands fall between 1350 and 1450 cm⁻¹.

For the aromatic ketones, the peak with the strongest intensity in the 1200–1300 cm⁻¹ range is due to a δ_{CH} mode which is coupled, in most cases, with the CH₂ wag. For Anth this peak falls short of 1300 cm⁻¹ and for Py the position ranges between 1240 and 1280 cm⁻¹. As shown in Figure 3, B$_{ghi}$P has several peaks with similar intensities between 1200 and 1400 cm⁻¹. The strongest aromatic ketone band, the C=O stretch, generally falls in the 1600–1700 cm⁻¹ region, the region obscured by the H−O−H bending mode in our experiments.

As shown in Figure 3 and discussed above, the frequencies of various functional groups can be distinct for a single molecular species. However the mid-IR region becomes increasingly complex when the possibility exists for multiple photoproducts to form, as is the case here. Given the overlapping functional group vibrational frequencies, we have utilized various data reduction techniques to extract as much information as possible from the experimental spectra in this region. These techniques, described below, include correlation plots comparing various photolysis-induced band growth rates. If separate, distinct bands are correlated in their growth rates, they are assumed to come from the same photoproduct.

3.2. Experimental Results

3.2.1. PAH Neutral and Photoproduct Spectra

As shown below, many of the theoretical photoproduct spectra discussed in Section 3.1 contain bands which either overlap with, or are very close to, other photoproduct bands in the IR windows accessible to our investigation (i.e., 1000–1650 cm⁻¹). This is due to the fact that this region corresponds to the C−C and C–H in-plane motions. In addition, the intensity of these bands is significantly increased by heteratom substitution, sidegroup addition, or ionization (Langhoff 1996;

Table 2
Pyrene Photoproduct Bands

Position (cm^{-1}) H_2O	Position (cm^{-1}) Argon[a]	I. A. in H_2O after 15 minutes of UV[b]	Theoretically Predicted Bands within $\pm/-20$ cm^{-1} of measured position in H_2O[c]	Band Strengths of Theoretical Bands (km/mol)	Possible Photoproduct Species (modes: δ, x, ν)
492	–	0.0014	–	–	–
658	–	0.0016	–	–	–
1128		0.0010	1147 (OH)	29	p3
1142		0.0020	1143, 1147(OH)	64, 29	p5, p3
1202		0.0044	1210, 1212(OH)	45, 96	p4$^\delta$, p3$^\delta$
1216	1216	0.0060	1210, 1212(OH)	45, 96	p4$^\delta$, p3$^\delta$
1232		0.0149	1237 (+), 1231, 1234 (OH)	78, 49, 38	+, p5$^\delta$, p3
1247	1245.1	0.0050	1237 (+), 1244 (CO)	78, 147	+, p6
1318		0.0010	1308 (OH)	79	p3^x
1340		0.0008	1334 (OH), 1334 (CO)	57, 31	p4^x, p10
1359	1358.4, 1361.8	0.0050	1350 (+)	132	+
1394		0.0049	1410 (CO)	30	p8
1446	1440.3	0.0020	1436 (+), 1461 (CO)	32, 33	+, p11
1483		0.0019	1482 (CO)	45	p7
1553	1550.9, 1553.4, 1556.0	0.0040	1550 (+), 1542, 1555 (CO)	191, 66, 31	+, p6, p12
1717	–	0.0017	1664 (OH), 1675, 1687 (CO)	232, 293, 230	p11, p10, p13, H_2CO[d]
2138	–	0.0013	–	–	CO
2277	–	0.0006	–	–	
2341	–	0.0409	–	–	CO_2
2850	–	0.0122	–	–	H_2CO, other aliphatics

Notes. Theoretical spectra from 1650–1000 cm^{-1} are shown in Figure 3. The abbreviation I.A. stands for integrated absorbance.
[a] From Bouwman et al. (2011a). Columns with a "–" were not reported or sought in Bouwman et al. (2011a).
[b] The integrated absorbances (I.A.) reported here correspond to the Py:H_2O = 1:110 mixture.
[c] Only predicted bands with band strengths >30 km mol^{-1} are reported.
[d] CO stretch of H_2CO has a band strength of 9.6e-18 cm per molecule, from Schutte et al. (1996).
[δ] δ_{O-H} band.
[x] X_{sens} band.

Bauschlicher & Langhoff 1997; Mattioda et al. 2003, 2005; Hudgins et al. 2005). The PAH electron distribution is disrupted in all cases, resulting in larger dipole derivatives associated with the vibration of the C−C and C−H in-plane modes.

To narrow down the identity of specific photoproducts, we focus on vibrational regions that are specific to certain photoproduct chemical classes and seek correlations between bands belonging to a specific photoproduct. As noted in Section 3.1 and Figure 3, the overlap of predicted photoproduct bands makes them challenging to distinguish in experimental spectra. The panels above the experimental spectra in Figure 4 illustrate this: cations, alcohols, ketones, and quinones have many bands with very similar frequencies. In each panel, vertical lines represent the positions of theoretically predicted bands. Red, cyan, and gray lines represent predicted positions of cations (PAH$^+$), alcohols (PAH(OH)$_n$), and quinones and ketones (PAH(O)$_n$), respectively. Only theoretically calculated bands with strengths larger than ∼30 km mol^{-1} are included; we do not expect to be able to detect many of the weaker (<30 km mol^{-1}) bands in our experimental spectra. The positions of these vertical lines correspond directly to the positions shown in Figure 3, and listed in Tables 1–3. These serve to illustrate the wide range of possibilities for assignment of the actual photoproducts.

Each panel of Figure 4 shows spectra of neutral, photolyzed, and neutral-subtracted (photolyzed spectrum minus neutral spectrum) PAH:H_2O ice samples for both a low- (black traces) and high- (blue traces) PAH concentration case. Photoproduct bands are detected most strongly in ice mixtures with low PAH concentrations. As Figure 4 shows, many of the photoproduct bands are not detectable at high PAH concentrations, perhaps

due to very low abundance (not necessarily absence) in those ices. Despite the crowding of theoretical band positions, some conclusions can be drawn from the experimental spectra.

The first column of Tables 1–3 lists the photoproduct bands (including cations) in H_2O ice, and the second column shows the corresponding wavelengths of those photoproducts in argon matrices, reported by Bouwman et al. (2011b). Note that bands tend to shift depending on the surrounding matrix material.

In the third column of Tables 1–3, we list theoretically predicted bands (only those with band strengths $A > 30$ km mole^{-1}) within ±20 cm^{-1} of the detected photoproduct bands. The fourth column lists the band strengths for each of the theoretical bands. Presumably, species with larger band strengths contribute more significantly to the detected photoproduct bands. The possible assignments for detected photoproducts are listed in the final columns of Tables 1–3. These are not unambiguous assignments. The abbreviations refer to the theoretical structures and spectra shown in Figures 1 and 3.

3.2.1.1. Anthracene

Low- and high-concentration anthracene spectra in Figure 4(a) correspond to monomer fractions of 28% and 0% respectively (computed as described in Section 3.2.1). Two of the cation bands are somewhat isolated, i.e., not crowded by other predicted photoproduct bands, falling at 1542 cm^{-1} and 1584 cm^{-1}. The corresponding experimental band positions in H_2O ices are at 1541 and 1589 cm^{-1}. These cation bands appear most clearly in the experimental spectra of the photolyzed, Anth:H_2O low PAH concentration ices (e.g., top black trace). Evidence for these cation bands in the Anth:H_2O high PAH concentration ices (e.g., top blue trace) is very weak.

Table 3
Benzo[ghi]perylene Photoproducts

Position (cm⁻¹) H₂O	Position (cm⁻¹) Argon[a]	I. A. in H₂O after 15 minutes of UV[b]	Theoretically Predicted Bands within ±/−20 cm⁻¹ of measured position in H₂O[c]	Band Strengths of Theoretical Bands (km/mol)	Possible Photoproduct Species (modes: δ, x, ν)
586	–	0.0008	–	–	–
657	–	0.0042	–	–	–
1080		0.0035	1093, 1095, 1101 (OH)	56, 39, 63	b7, b7, b8
1128		0.0015	1127, 1120, 1135 (OH), 1125, 1123, 1112 (CO)	105, 30, 37, 32, 53, 37	b3$^\delta$, b4, b5, b10, b11, b13
1146	1140.2	0.0034	1127, 1135, 1165, 1152, 1155 (OH)	105, 37, 141, 31, 31	b3$^\delta$, b5, b6$^\delta$, b8, b8
1153		0.0023	1135, 1165, 1152, 1155 (OH)	36, 141, 31, 31	b5, b6$^\delta$, b8, b8
1223	1216.7	0.0392	1218, 1220 (+), 1224, 1232, 1234, 1207, 1208, 1211, 1216, 1228, 1213, 1232 (OH), 1207, 1228 (CO)	41, 32, 53, 47, 36, 61, 40, 56, 71, 45, 120, 32, 56, 44	+, +, b3, b3, b3, b4, b4, b6, b7, b7$^\delta$, b8$^\delta$, b8, b15, b17
1232	1223.4	0.001	1218, 1220 (+), 1224, 1232, 1234, 1216, 1228, 1213, 1232 (OH), 1228 (CO)	41, 32, 53, 47, 36, 71, 45, 120, 32, 44	+, +, b3, b3, b3, b7$^\delta$, b7, b8$^\delta$, b8, b17
1253		0.002	1234, 1272, 1232 (OH), 1266, 1270, 1269, 1259, 1272 (CO)	36, 88, 32, 78, 49, 52, 55, 89	b3, b5^x, b8, b9, b12, b13, b14, b17
1300	1311.9	0.0056	1311(+), 1302, 1286 (OH), 1305, 1284, 1318, 1282, 1295, 1287 (CO)	69, 31, 62, 37, 66, 45, 38, 40, 118	+, b3^x, b5$^\delta$, b9, b11, b13, b15, b15, b16
	1324.4		–	–	–
1339	1331.9	0.0096	1343, 1345 (+), 1346, 1335, 1343, 1346, 1321 (OH), 1340 (CO)	33, 107, 46, 42, 54, 76, 42, 55	+, +, b3^x, b4, b5, b6^x, b8^x, b12
1352	1350.2	0.0043	1343, 1345 (+), 1346, 1335, 1361, 1343, 1346 (OH), 1340 (CO)	33, 107, 46, 42, 30, 54, 76, 55	+, +, b3^x, b4, b4, b5, b6^x, b12
1403	1401.3	0.0067	1400 (+), 1383, 1413, 1388 (OH), 1384, 1399 (CO)	127, 32, 34, 33, 38, 40	+, b5, b7$^\nu$, b8, b13, b16
	1538.6	–	–	–	–
1550	1550.5	0.0038	1559 (+), 1541, 1558, 1565, 1564, 1541, 1564 (CO)	20, 68, 144, 125, 35, 39, 75	+, b12, b12, b13, b15, b16, b17
1578	1578.2	0.0239	1571 (+), 1558, 1565, 1564, 1572, 1564, 1598, 1598, 1571 (CO)	383, 144, 125, 35, 84, 75, 49, 47, 42	+, b12, b13, b15, b13, b17, b15, b16, b17
1717	–	0	1673 (CO)	344	b9, H₂CO[d]
2136	–	0.011	–	–	CO
2276	–	0.001	–	–	–
2341	–	0.0715	–	–	CO₂
2848	–	0.011	–	–	H₂CO, other aliphatics

Notes. Theoretical spectra from 1650–1000 cm⁻¹ are shown in Figure 3. The abbreviation I.A. stands for integrated absorbance.
[a] From Bouwman et al. (2011a). Columns with a "–" were not reported or sought in Bouwman et al. (2011a).
[b] The integrated absorbances (I.A.) reported here correspond to the B$_{ghi}$:H₂O = 1:310 mixture.
[c] Only predicted bands with band strengths >30 km mol⁻¹ are reported.
[d] CO stretch of H₂CO has a band strength of 9.6e-18 cm per molecule, from Schutte et al. (1996).
[δ] δ_{O-H} band.
[x] X$_{sens}$ band.
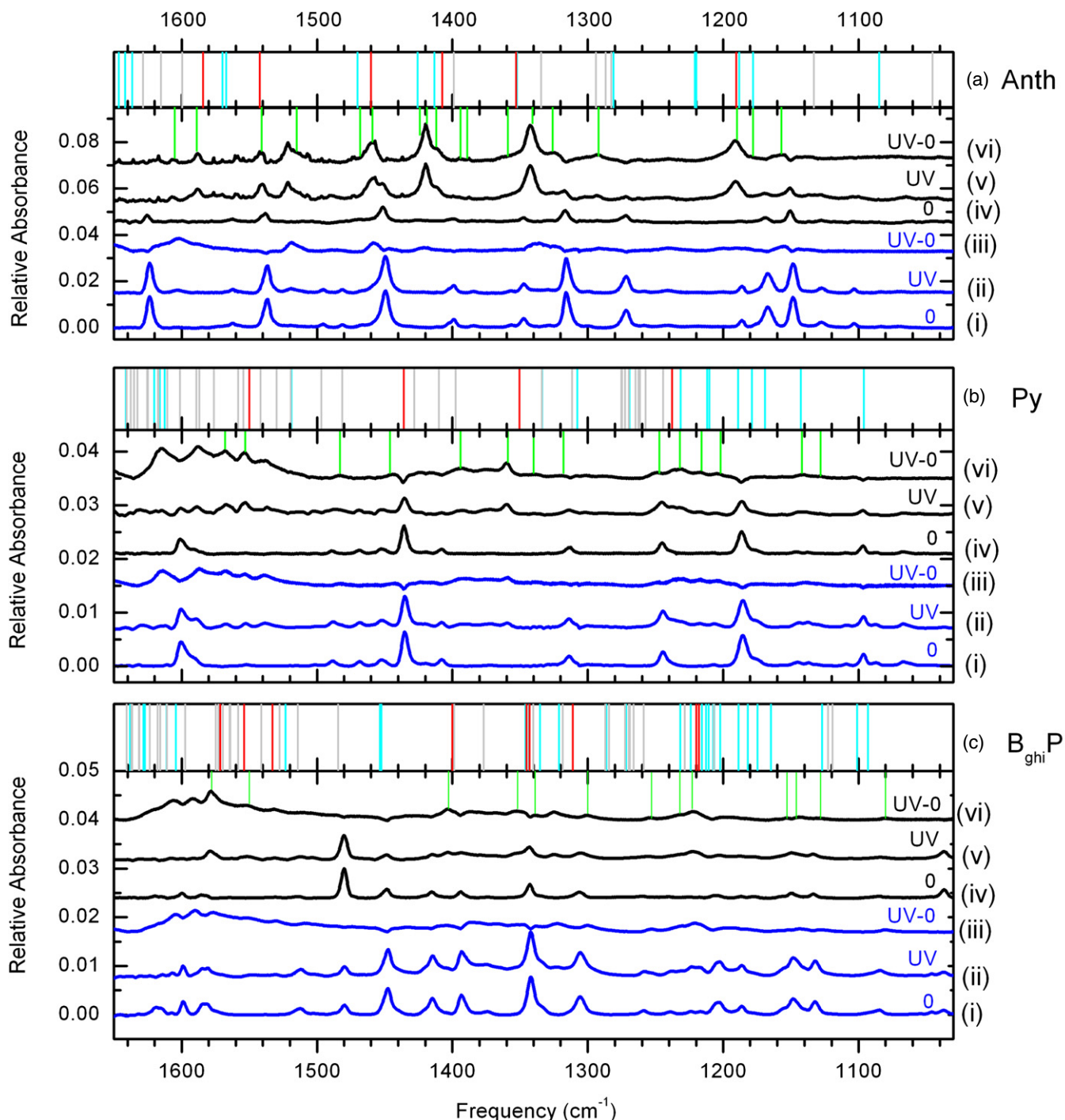[ν] $\nu_{C-C} + \delta_{C-H} + \delta_{O-H}$ band.

Figure 4. Laboratory IR spectra for neutral and UV-photolyzed PAH:H$_2$O ices: (a) black traces are Anth:H$_2$O 1:590 and blue traces are Anth:H$_2$O 1:20, (b) Py:H$_2$O 1:110 in black, and Py:H$_2$O 1:70 in blue, (c) B$_{ghi}$P:H$_2$O 1:310 in black, and B$_{ghi}$P:H$_2$O 1:70 in blue. The key to the spectra labels to the right of the plot are: (i)–(iii) neutral (0), photolyzed (UV) for 15 minutes, and neutral-subtracted (UV-0) high PAH concentration ice mixtures respectively; and (iv)–(vi) neutral, photolyzed for 15 minutes, and neutral-subtracted low PAH concentration ice mixtures, respectively. In the panels above each set of spectra, vertical red, cyan, and gray lines are the DFT computed positions of cation bands, PAH-derived alcohols, and PAH-derived ketones/quinones, respectively. Only computed band positions with predicted band strengths larger than ∼30 km mol^{-1} are included. The vertical green lines within the panels of spectra indicate positions of detected photoproduct features; other apparently "new features" that are unmarked by vertical lines are either the result of over-subtraction around strong neutral bands or due to baseline shift. See Section 2.2 for details on spectral subtraction and baseline determination.

Although the vertical red (cation) lines at 1190, 1352, 1407 and 1460 cm^{-1} overlap with cyan (OH-substituted) and gray (CO-substituted) lines, based on band strengths, we attribute the bulk of the 1190, 1340, 1419, 1459 cm^{-1} bands to the anthracene cation.

Apart from these few bands that can be assigned with reasonable confidence to the cations, bands that arise from the same species can be identified using correlation plots. This is illustrated in Figure 5, which shows that a correlation exists ($R = 0.98$) for the growth of the 1157 and 1326 cm^{-1} bands,
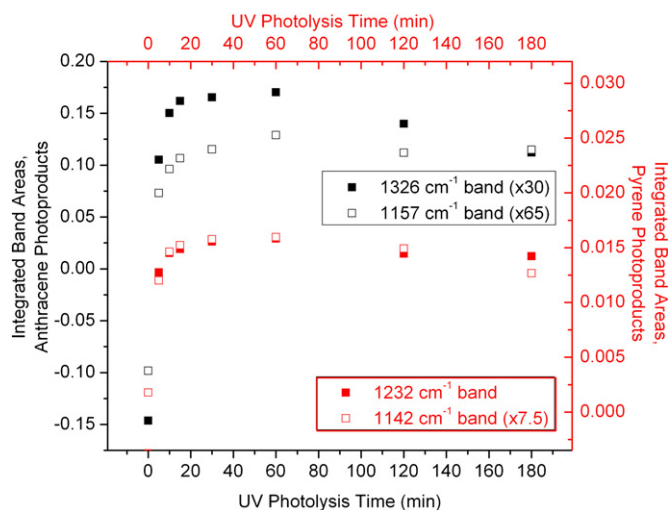
Figure 5. Example of how photoproduct correlations are identified. Black data points (and black axes) show similar growth patterns between the 1157 and 1326 cm^{-1} bands in photolyzed Anth; the correlation ($R = 0.98$) between these bands indicates that they form in tandem. Red data points (and red axes) show a similar kind of correlation in the growth of the 1142 and 1232 cm^{-1} bands in photolyzed Py ($R = 0.92$). See Section 3.2.1.1 for discussion.

at UV photolysis times of 10 through 180 minutes (black data points). Both of these bands appear to reach their maximum strength around 60 minutes of photolysis time, and then start to decrease. This correlation points to anthraquinone ("a8," from Figure 2) as the carrier.

Using similar correlation plots, the bands in H$_2$O at 1424 (shoulder) and 1468 cm^{-1} can be assigned to the theoretical bands at 1426 (OH) and 1469 (OH) cm^{-1} for 9-anthrol and 2-anthrol (a4 and a5). Likewise, the experimental bands at 1389, 1394 and 1459 cm^{-1} can be assigned to 1,4-dianthranone ("a7"). However, as we cannot detect the ν_{C-O} stretch band around 1660 cm^{-1} and the O−H stretch around 3600 cm^{-1} due to the overlap with the broad H$_2$O–ice features we cannot fully ascertain if these specific anthrols and anthrones are present. The formation of anthrols and anthranones in our experiments is consistent with the IR studies of Guennoun et al. (2011a, 2011b) who showed that the near-UV photolysis of pyrene and coronene with water in several matrices at low temperatures produced aromatic ketones and alcohols.

Several photoproduct bands also appear that are not directly PAH-related, but most likely come from PAH photolysis products. Bands due to CO$_2$ (2341 cm^{-1} asymmetric stretch and 649 cm^{-1} bending), CO (2136 cm^{-1}) and C$_3$O$_2$ (2275 cm^{-1}; Gerakines & Moore 2001), as well as a distinct features at 2850 cm^{-1} and 1717 cm^{-1} grow in with photolysis. These are discussed further in Sections 3.3 and 3.4.

3.2.1.2. Pyrene

Figure 4(b) shows the spectra for a 1:110 and a 1:70 Py:H$_2$O ice; both fall in the high PAH:H$_2$O concentration regime, with monomer fractions of 4% and 0%, respectively. Both sets of experimental spectra confirm the presence of the Py cation after photolysis; theory predicts Py$^+$ lines at 1237, 1350, 1436, and 1550 cm^{-1}, with the 1350 and 1550 cm^{-1} bands having the largest band strengths. We attribute the lines in our experimental spectra at 1247, 1359, and 1553 cm^{-1} to the cation as they are well within the uncertainties inherent in the theoretical predictions and the unknown shifts induced by the H$_2$O–ice matrix. The cation band predicted at 1436 cm^{-1} is not detected,

presumably because it falls in a region that is obscured by a strong, over-subtracted neutral Py band.

Table 2 also lists the noncation Py photoproduct bands, along with the theoretical lines that may correspond to those detections. Based on correlation plots as shown in Figure 5, all of the photoproduct bands below 1235 cm^{-1} appear to correspond to predicted positions for OH-substituted Py species (cyan lines in Figure 4(b)). Figure 5 shows that a correlation exists for the growth of the 1142 and 1232 cm^{-1} bands (red data points). The two bands appear to reach their maximum strength at about 60 minutes of photolysis time. The trends are tightly correlated, with $R = 0.92$, and both are theoretically associated with the 2-hydroxypyrene and 4-hydroxypyrene, "p5" and "p3" in Figure 1. These two hydroxypyrenes are among the three suggested by Guennoun et al. (2011a) as key intermediates in the formation of the ketone end products in their photochemical studies of Py:H$_2$O = 1:10, Py deposited on amorphous H$_2$O, and Py:H$_2$O:Ar (variable:1:50) deposited at 10 K followed by in situ photolysis with near UV radiation, $\lambda > 235$ nm.

Most of the Py photoproduct bands between 1320 and 1600 cm^{-1} are attributed to Py$^+$ and Py ketones. The bands at 1394 and 1483 cm^{-1} can be attributed to two forms of 4-pyrenone, "p7" and "p8" in Figure 1. The 1318 cm^{-1} band can be attributed to the PyOH band at 1308 cm^{-1} (p3). The band at 1340 cm^{-1} has contributions from both PyOH and Py=O.

As with anthracene, several photoproduct bands also appear in the Py:H$_2$O ices that are not directly PAH-related, but probably come from PAH photolysis products. Bands due to CO$_2$ (2341 cm^{-1} asymmetric stretch and 649 cm^{-1} bending), CO (2136 cm^{-1}) and C$_3$O$_2$ (2275 cm^{-1}; Gerakines & Moore 2001), as well as distinct features at 2850 cm^{-1} and 1717 cm^{-1} grow in with photolysis. These are discussed further in Sections 3.3 and 3.4.

3.2.1.3. Benzo[ghi]perylene

Figure 4(c) shows the spectra for low- and high-concentration B$_{ghi}$P:H$_2$O ices, with monomer fractions of 28% and 0% respectively. Due to the larger size of the molecule, and its more complex molecular structure, more possibilities exist for OH and CO isomers than for anthracene and pyrene. Consequently, significantly more photoproduct bands are expected, as reflected in the panel above the spectra, which is quite crowded compared to the corresponding panels for Anth and Py.

All eight of the predicted cation bands at 1218, 1220, 1311, 1343, 1345, 1400, 1559, and 1571 cm^{-1} are visible in the photolyzed spectra. As with the Anth:H$_2$O ices, the B$_{ghi}$P cation bands appear most clearly in low concentration B$_{ghi}$P:H$_2$O ices (e.g., top black trace). We tentatively assign the predicted bands to the following experimental bands that grow with photolysis: 1223, 1232, 1300, 1339, 1352, 1403, 1550, and 1578 cm^{-1}. However, note that the experimental bands may also be partially explained by the presence of other photoproducts. A good example is the photoproduct band at 1300 cm^{-1}. While a cation band is predicted at 1311 cm^{-1}, there are also many other species, primarily ketones, that have bands in this region that could overlap with the cation band. The largest band strength of a predicted feature that lies within ±20 cm^{-1} of the detected band, is 118 km mol^{-1}. It is from 1,6-benzo[ghi]perylene-one, at 1287 cm^{-1} ("b16" in Figures 1 and 3).

All the photoproduct bands listed in Table 3 between 1080 and 1153 cm^{-1} are due to B$_{ghi}$P–OH photoproducts. Based on band strengths and correlations like those shown in Figure 5, the b3 and b6 forms shown in Figure 1 are expected to be the
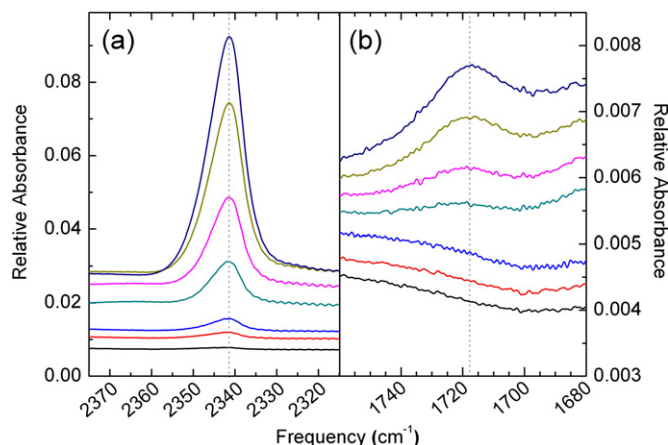
Figure 6. Spectra of Anth:H_2O (1:260) showing the growth of (a) the 2341 cm^{-1} CO_2 band and (b) the 1717 cm^{-1} H_2CO band with increasing photolysis time. See Sections 3.3 and 3.4 for discussion.

dominant alcohols. The experimental band at 1253 cm^{-1} can be attributed to both B$_{ghi}$P–OH and B$_{ghi}$P=O photoproducts.

As with anthracene and pyrene, several photoproduct bands also appear in the B$_{ghi}$P:H_2O ices that are not directly PAH-related, but likely come from PAH photolysis products. Bands due to CO_2 (2341 cm^{-1} asymmetric stretch and 649 cm^{-1} bending), CO (2136 cm^{-1}) and C_3O_2 (2275 cm^{-1}; Gerakines & Moore 2001), as well as distinct features at 2850 cm^{-1} and 1717 cm^{-1} grow in with photolysis. These are discussed further in Sections 3.3 and 3.4.

3.3. CO₂ Formation Yield as a Proxy for PAH Erosion

As discussed in Section 3.1 and illustrated in Figure 2, in addition to stable aromatic alcohol and ketone formation, PAH oxidation by the water photoproducts, O and OH, can lead to edge ring rupture and, ultimately, CO production within the ice. This CO can then react with the water photoproduct, OH, to form CO_2 and release H (Noble et al. 2011). Therefore, CO_2 production can be used as a proxy for PAH photo-decomposition, unlike the formation rates of aromatic alcohols and ketones, which track PAH modification. We use the 2341 cm^{-1} CO_2 band to track this process instead of the 2143 cm^{-1} band due to the primary photoproduct CO for three reasons. The 2341 cm^{-1} CO_2 band is clear and unperturbed in all of the photolysis spectra, it possesses an extraordinarily large integrated band strength ($A_{CO_2} \sim 2 \times 10^{-16}$ cm molecule^{-1} versus $A_{CO} \sim 1 \times 10^{-17}$ cm molecule^{-1}, e.g., Hudgins et al. 1993 and references therein.), and CO_2 seems to be the major end product. Figure 6(a) shows the growth of this band with photolysis in the Anth:$H_2O = 1:260$ ice. Figure 7 shows the growth in the integrated area of this band plotted versus photolysis time for the different PAH:H_2O concentrations studied. The first observation to be drawn from these plots is that, regardless of the PAH:H_2O ratio, CO_2 abundance increases with increasing photolysis time.

This behavior is similar to a trend observed by Oba et al. (2010) for the production of CO_2 from CO molecules and OH radicals codeposited onto an aluminum substrate at different temperatures. At substrate temperatures of 10 K and 20 K, they observed a growth in CO_2 up to a saturation point, an effect that they attributed to the very low mobility of CO and OH on the surface at temperatures below 20 K, and by the growth in the number of trapping sites in the H_2O ice layer that form during their experiments.
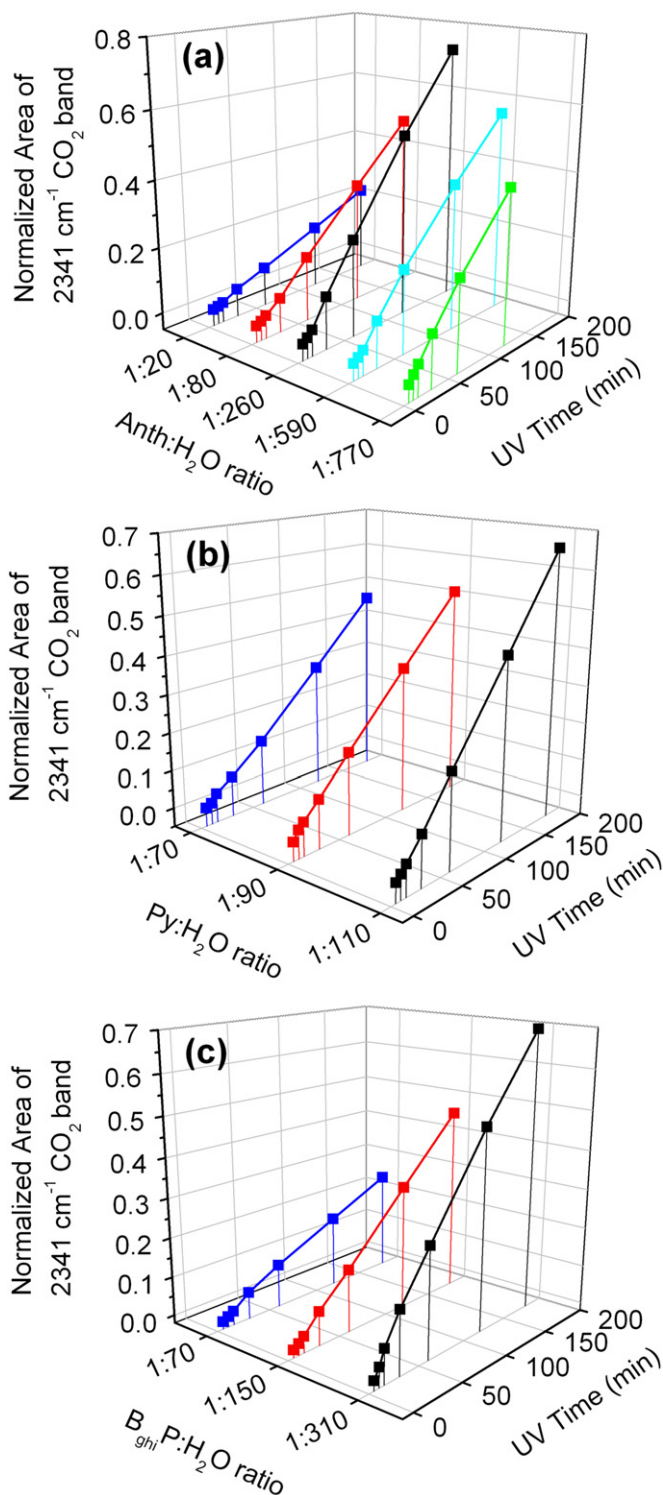

Figure 7. Growth of the 2341 cm^{-1} CO_2 band with photolysis time, for all PAH:H_2O ice ratios studied here. All growth curves have been normalized to zero band area at 5 minutes of UV exposure. For PAH:H_2O ratios above about 1:300, lowering PAH concentrations results in higher CO_2 production rates and hence higher erosion rates for the PAHs. However, panel (a) reveals that for even lower PAH concentrations, CO_2 formation drops.

The second conclusion to be drawn from the plots in Figure 7 is that the rates of CO_2 production *increase* with *decreasing* PAH:H_2O concentration (that is, with more H_2O) for all three PAHs, when concentrations range from tens of water molecules per PAH molecule to ~300 water molecules per PAH molecule.

Table 4
Slopes of the Growth of the 2341 cm^{-1} CO$_2$ Band Area as a Function of Photolysis Time and Concentration Shown in Figure 6

Anth:H$_2$O ratio	Slope (cm^{-1} min^{-1})	Py:H$_2$O ratio	Slope (cm^{-1} min^{-1})	B$_{ghi}$P:H$_2$O ratio	Slope (cm^{-1} min^{-1})
1:20	0.0013	⋯	⋯	⋯	⋯
1:80	0.0028	1:70	0.0026	1:70	0.0014
⋯	⋯	1:90	0.0029	⋯	⋯
⋯	⋯	1:110	0.0038	1:150	0.0026
1:260	0.0042	⋯	⋯	1:310	0.0039
1:590	0.0033	⋯	⋯	⋯	⋯
1:770	0.0036	⋯	⋯	⋯	⋯

Table 4 lists the slopes derived from linear fits to the data shown in Figure 7. Perusal of Figure 7 shows anthracene and benzo[ghi]perylene exhibit a similar, almost linear, absolute CO$_2$ growth pattern, with increasing slope values (see Table 4) from a PAH:H$_2$O concentration of 1:20 to about 1:300. The CO$_2$ growth curves for pyrene show similar, but much less marked behavior, presumably because they span a smaller concentration range. After 3 hr of UV irradiation, roughly 10% of the total number of carbon atoms available in the Anth:H$_2$O (1:260) ice is converted to CO$_2$. At the start of the experiment there were 6.3×10^{15} Anth^0 cm^{-2}. Since Anth contains 14 carbon atoms, the carbon atom reservoir is 8.8×10^{16} cm^{-2}. After 3 hr of photolysis, 2.5×10^{15} neutral anthracene molecules remain (40% of the starting amount) and 10^{16} CO$_2$ molecules have formed.

The results for anthracene shown in Figure 7(a) (see also Table 4) indicate that the trend of steepening slopes peaks for PAH:H$_2$O concentrations between about 1:300 and 1:600. For Anth:H$_2$O = 1:590 and 1:770, the CO$_2$ production rate drops by about 10% at each step. After 2 hr of UV irradiation, roughly 1% of the total number of carbon atoms available in the Anth:H$_2$O (1:770) ice are converted to CO$_2$. At the start of the experiment there were 2.7×10^{17} Anth^0 cm^{-2}. Since each Anth molecule contains 14 carbon atoms, the carbon atom reservoir is 3.9×10^{18} cm^{-2}. After 2 hr of photolysis, 2.7×10^{15} neutral anthracene molecules remain ($\sim$1% of the starting amount) and 5×10^{15} CO$_2$ molecules have formed.

Unfortunately, the studies for pyrene and benzo[ghi]perylene were limited to higher PAH concentrations, so any turning points with respect to lower PAH concentration were not measured for these species.

3.4. The Unusual 2850 cm^{-1} Band

Figure 8 shows the 3100–2700 cm^{-1} region of the spectra for several Anth-, Py-, and B$_{ghi}$P- H$_2$O ice mixtures to illustrate that a weak, broad feature centered near 2850 cm^{-1} grows in with increasing photolysis time. The feature spans the region from 2900 to 2800 cm^{-1} (FWHH $\sim$ 50 cm^{-1}) and is evident, in varying strength, at all concentrations for the three PAHs studied. Figure 9 plots the integrated band area of this feature versus photolysis time for the different Anth:H$_2$O concentrations studied, similar to the presentation of the 2341 cm^{-1} CO$_2$ band in Figure 7. In preparing Figure 9, all band areas for each concentration are normalized to the area of the band after five minutes of photolysis, when the band first appears. Since production of the 2850 cm^{-1} band carrier is very low in the high PAH concentration ices, the data sets for the higher PAH concentration cases have the largest errors due to the inherent difficulty in establishing a stable baseline. The overall trend indicates that the 2850 cm^{-1} band grows very slowly (if at all) with decreasing Anth concentration from Anth:H$_2$O = 1:20 to 1:260, and that it

jumps dramatically between Anth:H$_2$O = 1:260 and 1:590. Similar behavior is found for the high PAH concentration, Py:H$_2$O and B$_{ghi}$P:H$_2$O ices. As noted above, the studies for pyrene and benzo[ghi]perylene were limited to higher PAH concentrations, so any turning points with respect to lower PAH concentration were not measured for these species.

While both the 2850 and 2341 cm^{-1} bands are clearly associated with PAH photoproducts, comparing the behavior of the 2850 cm^{-1} band for the anth:H$_2$O ices in Figure 9 with the behavior of the 2341 cm^{-1} band in Figure 7 indicates that CO$_2$ and the 2850 cm^{-1} band carrier form by very different reaction networks that appear to be associated with either high or low PAH concentration ices. After 3 hr of UV irradiation for all high PAH concentration ices (PAH:H$_2$O 1:18 to 1:310) studied, the 2850 cm^{-1} feature is barely discernable, reaching a maximum, normalized "band" area of less than 0.02. In contrast, the 2341 cm^{-1} CO$_2$ band reaches a maximum that is between a factor of 10 and 40 times higher in these same ices. For the low concentration Anth:H$_2$O = 1:593 and 1:765 ices, the behavior reverses, with the 2850 cm^{-1} feature growing two to three times faster while CO$_2$ production efficiency drops by some 10%. Since the 2850 cm^{-1} band falls in the region associated with CH stretching vibrations, its carrier must be produced by the reaction of PAHs and PAH photoproducts with H radicals. However, as shown below, the chemical nature of the carrier is far from clear.

While at first glance the 2850 cm^{-1} feature suggests a run-of-the-mill aliphatic carrier, close inspection rules out pure aliphatic hydrocarbons. The top spectrum in Figure 8(c) shows that the band is structureless, with endpoints that break from the continuum near 2910 and 2780 cm^{-1}. This is not consistent with aliphatic materials containing methyl and methylene groups. The symmetric and asymmetric CH stretching modes in methyl (-CH$_3$) and methylene (-CH$_2$-) groups give rise to four bands between roughly 2980 and 2840 cm^{-1}, with the strongest lying between 2910 and 2980 cm^{-1}, well outside the range of the 2850 cm^{-1} feature (e.g., Bellamy 1958; Silverstein & Bassler 1963). This holds for methyl- and methylene- containing materials in the gas phase, condensed as low temperature solids, and trapped in water-rich ices (e.g., d'Hendecourt et al. 1986; Allamandola et al. 1988 and references therein). This also holds for cyclic aliphatics such as cyclo-hexane (d'Hendecourt et al. 1986 and references therein) and hydrogenated PAHs (H$_n$-PAHs) containing both aromatic and aliphatic carbons (Bernstein et al. 1996). While it cannot be ruled out as cleanly as these other aliphatic groups, the CH stretch associated with tertiary CH groups in pure aliphatic materials being responsible for the 2850 cm^{-1} feature is highly unlikely. The peak position is a little off, 2880 cm^{-1} versus 2850 cm^{-1} (Bellamy 1958; Allamandola et al. 1992 and references therein) and, more importantly, it is difficult to reconcile the observation that the 2850 cm^{-1} band is strongest in the dilute
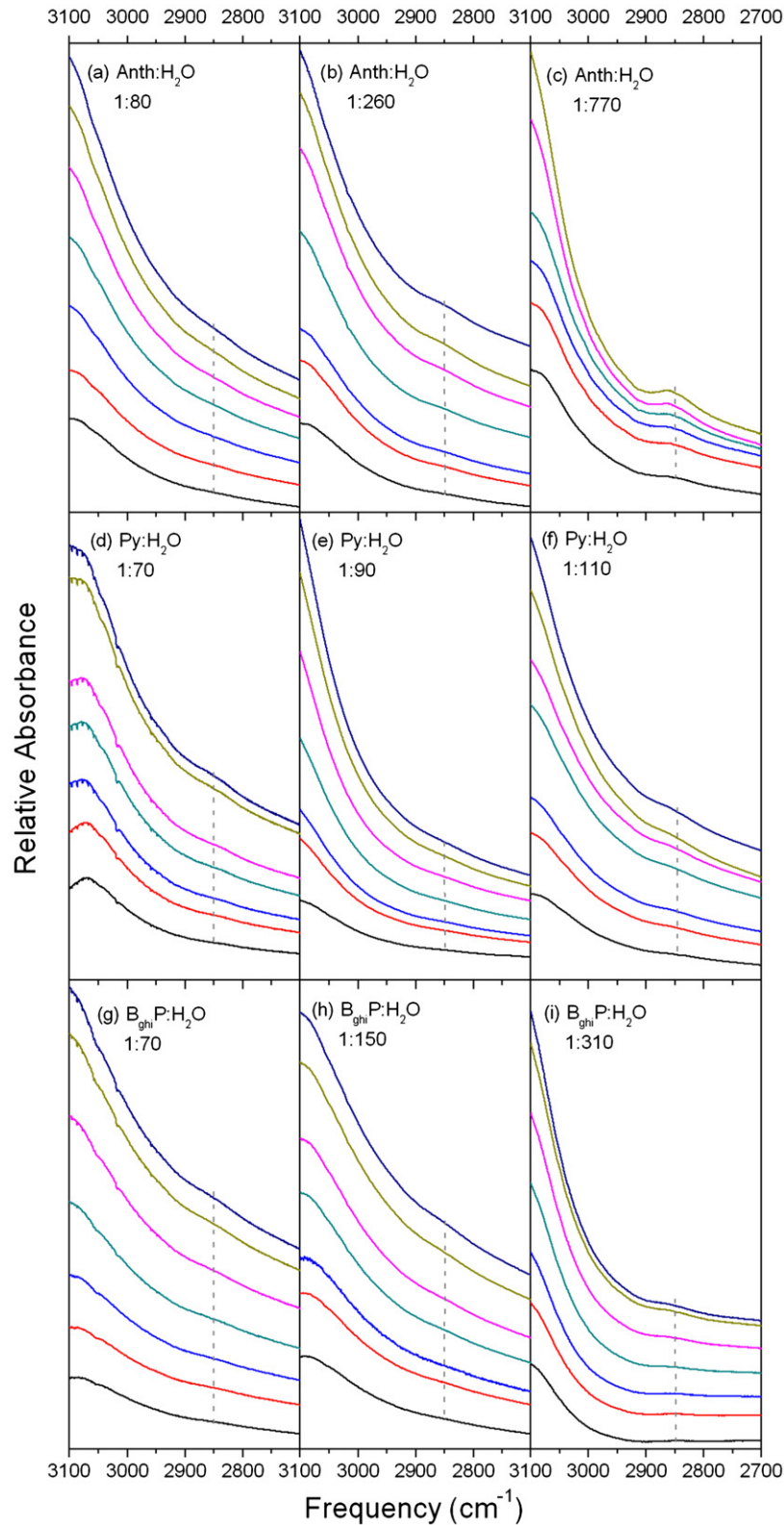
Figure 8. 3100–2700 cm^{-1} spectra of different PAH:H$_2$O ices showing the growth of the 2850 cm^{-1} feature as a function of UV photolysis time. Black, red, blue, cyan, magenta, chartreuse, and navy traces are spectra measured at 5, 10, 15, 30, 60, 120, and 180 minute photolysis times, respectively. Panels (a)–(c) show neutral-subtracted anthracene:H$_2$O ices. Panels (d)–(f) show neutral-subtracted pyrene:H$_2$O ices. Panels (g)–(i) show neutral-subtracted benzo[ghi]perylene:H$_2$O ices. Note that the more dilute the PAHs mixtures are, the more pronounced the 2850 cm^{-1} bands are. See Section 3.4 for discussion.

anthracene experiments since anthracene has only 4 tertiary carbons while pyrene and benzo(ghi)perylene have 6 and 9, respectively. We have found but one example of a hydrocarbon that can produce such a feature. All the bands of the unusual hydrocarbon 1,4,5,8,9,10-hexahydroanthracene that fall in the aliphatic CH stretching region lie between 2900 and 2800 cm^{-1} (Figure 9 in Sandford et al. 2013). As with tertiary CH, we also consider this type of unusual fused ring compound as the
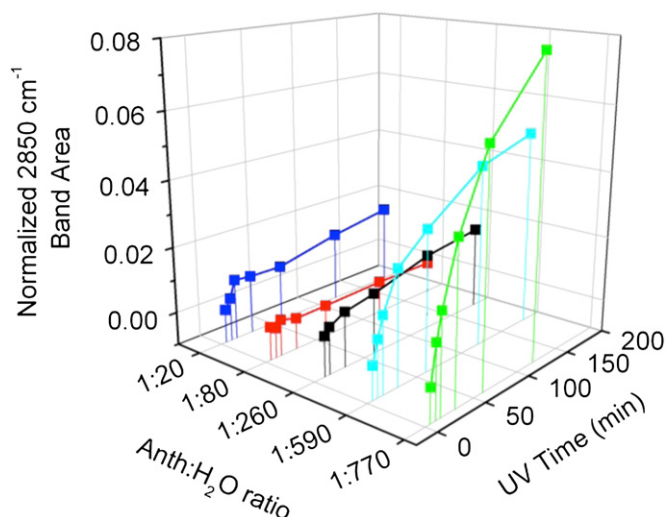
Figure 9. Growth of the 2850 cm^{-1} photoproduct feature with photolysis time, for each Anth:H$_2$O ratio. All growth curves have been normalized to zero band area at five minutes of UV time. Anthracene shows a pronounced increase in the 2850 cm^{-1} band area for PAH:H$_2$O concentrations between 1:260 and 1:590.

carrier of the 2850 cm^{-1} highly unlikely. Inspection of aliphatic groups adjacent to unsaturated groups such as carbonyls and double bonded carbon can also be ruled out (Silverstein & Bassler 1963).

Aldehydes are another type of chemical subgroup that could be responsible for the 2850 cm^{-1} feature because their CH stretching bands fall between 2900 and 2700 cm^{-1} (e.g., Bellamy 1958; Silverstein & Bassler 1963). However, they have two bands of roughly equal intensity in this region, with one generally falling between 2760 and 2790 cm^{-1}, outside the envelope of the 2850 cm^{-1} feature. For example, the bands for the simplest aldehyde, formaldehyde (H$_2$CO), fall at 2843 and 2766 cm^{-1} when it is in the gas phase (van der Zwet et al. 1985 and references therein). While this suggests H$_2$CO is not responsible for the 2850 cm^{-1} feature, these bands undergo unusually large blueshifts when the molecule is trapped in different ices. They fall at 2853 and 2785 cm^{-1} when it is frozen in water ice at 10 K, and at 2896 and 2835 cm^{-1} when it is trapped in a mixed molecular, cosmic ice analog comprised of H$_2$CO:NH$_3$:H$_2$O:CO$_2$:CO (1:1:3:5:10) at 10 K(van der Zwet et al. 1985). Associated (solid) H$_2$CO, produces bands at 2886 and 2823 cm^{-1} (van der Zwet et al. 1985 and references therein). Speculating, it therefore seems plausible that H$_2$CO and closely related species containing an aldehydic subgroup could be trapped in different sites within the photolyzed ice, with each site inducing slightly different shifts. Band blending could then produce a broad feature that coincides with and contributes to the envelope of the unusual 2850 cm^{-1} feature. This possibility can be tested because formaldehyde possesses four other IR active modes, with two very strong bands in H$_2$CO:H$_2$O = 100:3 ices at about 1720 and 1500 cm^{-1} and two weak bands near 1245 and 1175 cm^{-1} (Schutte et al. 1993). The 1719 cm^{-1} integrated band strength is 2–5 times larger than that of the CH stretching bands at 2886 and 2883 cm^{-1}, while the 1496 cm^{-1} band is of comparable strength. Since the integrated strengths for the 1245 and 1175 cm^{-1} bands are less than half that of the CH stretching bands, detecting the formation and growth of a band near 1720 cm^{-1} would support the suggestion of associated H$_2$CO being responsible for the 2850 cm^{-1} feature.

Figure 6(b) shows that a distinct band near 1720 cm^{-1} indeed grows in with photolysis. Band–band correlation plots as discussed above show the band near 1720 cm^{-1} correlates with both CO and CO$_2$ growth, behavior that is required if the 1720 cm^{-1} band originates in H$_2$CO because it and CO$_2$ form from CO. If this indeed originates with H$_2$CO, a weak feature near 1500 cm^{-1} should be evident. The UV-photolyzed spectra for the anth:H$_2$O ice experiments in Figure 4 show the growth of a broad, structured feature between 1500 and 1530 cm^{-1} with FWHH $\sim$ 10 cm^{-1}. The panel of computational photoproduct spectra above the experimental spectra shows this feature falls in a region that is devoid of predicted anthracene photoproduct bands. The blueshift and breadth of the broad feature centered near 1515 cm^{-1} is consistent with an origin in the types of H$_2$CO complexes that produce the broad 2850 cm^{-1} feature because both modes involve CH vibrations; that at 2850 cm^{-1} is produced by shifting and overlapping of the symmetric and asymmetric CH stretches (ν_1 and ν_4) and that near 1500 cm^{-1} by the CH$_2$ scissoring vibration (ν_3). In view of this, together with the observation that this feature is strongest and most clear in the anthracene experiments, in which the 2820 cm^{-1} band is most distinct, we tentatively ascribe both the 1720 and 1520 cm^{-1} bands to complexed formaldehyde. While the growth of the 1720 cm^{-1} band is clear for the other PAH:H$_2$O ices studied here, the case for the 1520 cm^{-1} band is not as clearcut for these PAHs because this region is rich in parent and photoproduct bands (see Figure 4).

4. DISCUSSION

4.1. The Importance of PAH Cations and the Role of PAH Concentration in Determining Bulk Ice Reactions

Before discussing the results presented in Section 3, it is important to put them in the context of what is already known about the affects of PAH concentration on PAH photochemistry, PAH isolation, and PAH clustering in low temperature water ice. First, consider PAH photolysis in water ice. Recent, elegant, laser desorption/ionization-TOF experiments (Gudipati & Yang 2012; Yang & Gudipati 2014), coupled with earlier UV–VIS spectroscopic studies show that immediately upon photolysis, in situ PAH ionization and stabilization is facile and rapid, with ionization yields and final products within the ice strongly dependent on ice composition, temperature, photolysis duration (Gudipati & Allamandola 2003, 2006; Bouwman et al. 2010, 2011b), and PAH concentration (Bouwman et al. 2011a; Cuylle et al. 2014). The reasons for strong PAH ionization and possible PAH cation reaction pathways with H$_2$O radical photoproducts (H and OH) in UV photolyzed water ice are discussed in great detail elsewhere (Gudipati & Allamandola 2003; Woon & Park 2004; Gudipati & Allamandola 2006; Bouwman et al. 2010, 2011a). Regarding concentration, careful studies by Cuylle et al. (2014) have shown that ionization efficiency *increases* with *decreasing* PAH:H$_2$O concentration. They show that ionization efficiency increases from 15% at concentrations of 1:1000 and higher to over 60% at very low concentrations of less than 1:10,000. The concentrations of most of the ices studied here fall in the 15% ionization efficiency range. However, the two most dilute Anth:H$_2$O ices (1:770 and 1:590) fall in the transition region described by Cuylle et al. Since anthracene is smaller than the PAHs studied by Cuylle et al., at these concentrations, it likely has a higher monomer fraction and, therefore, slightly higher ionization efficiency.

As the PAH concentration increases from the most dilute cases studied, the fraction of PAH monomers to PAH aggregates and clusters trapped within the ice decreases. As mentioned earlier in Section 2.3.2, our simple matrix isolation model suggests that the monomer fraction for anthracene drops from approximately 67% for Anth:H_2O = 1:770 to 0.4% for Anth:H_2O = 1:80. Similarly, the pyrene monomer fraction is computed to drop from approximately 4% for Py:H_2O = 1:110, to 0% for Py:H_2O = 1:70. For benzo[ghi]perylene, the monomer fraction is computed to fall from 28% from B_{ghi}P:H_2O = 1:310, to 0% for B_{ghi}P:H_2O = 1:70.

We now discuss the results presented in Figure 7 and Table 4, considering first the high PAH concentration behavior up to PAH:H_2O ∼ 300 for all three PAHs and then the two low anth:H_2O concentrations (Anth:H_2O = 1:590 and 1:770).

High PAH Concentration. All the PAH:H_2O > 1:300 experiments discussed here fall in the low PAH monomer and low PAH ionization fraction (5%–15%) regime described by Cuylle et al. (2014). Neutral PAH reaction networks such as shown in Figure 2, along with similar studies of neutral PAHs with H and OH (Dauben et al. 1975; Watanabe & Kouchi 2002; Oba et al. 2010; Noble et al. 2011; Giuliano et al. 2012), suggest PAH complexes and neutral PAHs dominate the chemistry that produces CO_2. Perhaps the increase in the CO_2 production slope as the PAH concentration decreases can be rationalized in terms of the increase of PAH monomer fraction. PAH monomers will be more reactive than the equivalent PAH moieties comprising the clusters simply because each PAH has more sites which are available for attack by excited OH and H radicals. Furthermore, besides having fewer sites available, PAH clusters should also be less reactive than the monomers due to shielding from the π-electrons. Thus, the more PAH monomers available, the greater the ultimate CO_2 yield, but only up to a point. The similarity in the slopes for the pyrene case, which samples a restricted concentration range, supports this picture. However, if the fraction of PAH monomers is the only important factor determining the slope, the trend of increasing slope should continue for the two lower concentration anthracene studies. But, as shown in Figure 7(a), it does not. Instead, as discussed below, an entirely different reaction network becomes dominant as PAH concentration drops below roughly 1:300.

Low PAH Concentration. In a recent study of the role temperature plays in PAH:H_2O ice photochemistry, Bouwman et al. (2010) found that there are two distinct reaction pathways. At low temperatures (<50 K), the chemistry is largely governed by ion–molecule interactions and processes, and at temperatures above 50 K, reactions are dominated by diffusing radical species. We attribute the distinctly different behavior in CO_2 production at high and low concentrations similarly, namely the low PAH concentration case (PAH:H_2O < 1:300) favors PAH ion-driven and ion-dominated reaction networks and processes while the high concentration case (PAH:H_2O > 1:300) favors reaction networks dominated by neutral species. At face value, the two low-concentration Anth:H_2O studies (Anth:H_2O = 1:590 and 1:770) fall in the region where PAH ionization fraction starts to increase. However, as considered in the monomer fraction model used here because of its smaller size than the PAHs studied by Cuylle et al. (2014), the anthracene monomer fraction is higher than those at the equivalent concentrations for larger PAHs because it requires fewer water molecules to isolate from other trapped PAH molecules. In addition, determining PAH concentrations in water ice using experimental UV–VIS band strengths, Hardegree-Ullman et al. (2014) recently reported

that the vibrational band strengths for pyrene are 1.5 times higher than the theoretically computed values used in the earlier Bouwman et al. studies. If this is born out, and holds for PAHs in general, the anthracene concentration should be reduced by this factor as well, resulting in the Anth:PAH 1:590 case dropping to <1:890 and the 1:770 case to <1:1160. Taken together, these adjustments push the anthracene experiments into the region where the PAH cation fraction starts to increase significantly (Cuylle et al. 2014). The implication from the plots shown in Figure 7(a) is that once reaction networks initiated by ionized PAHs become important, the reaction scheme that results in PAH erosion and, ultimately, CO_2 production is quenched.

These results increase our understanding of the PAH–ice properties that determine the role concentration plays in PAH:H_2O ice photochemistry. At high PAH concentrations (PAH:H_2O > 1:1000) the chemistry is apparently dominated by neutral reactions that primarily involve water photoproducts OH and H. As the concentration lowers, two factors come into play. First the fraction of PAH monomers to PAH clusters and complexes grows, increasing the number of free PAH molecules that can react with the radicals H and OH produced by the UV photolysis of H_2O. Second, as PAH concentration drops below PAH:H_2O ∼ 1:1000, PAH ionization and stabilization becomes increasingly important because the number of H_2O molecules per PAH continually grows, providing an ever increasing number of sites to trap electrons and add the thermodynamic stability associated with the solvation energy of the isolated PAH cations (Gudipati & Allamandola 2006; Cuylle et al. 2014; Woon & Park 2004 and references therein).

Furthermore, Guennoun et al. (2011a, 2011b) showed that aromatic alcohols, ketones and quinones are formed by irradiating pyrene and coronene in low temperature H_2O ices, not with UV radiation, but with near-UV radiation (λ > 235 nm). This strongly supports the picture that PAH cations determine the photochemical pathways followed in PAH:H_2O ices. H_2O is transparent at wavelengths longer than about 220 nm, production of H and OH radicals is negligible at best, while PAH ionization—provided it is in water ice—occurs readily (Gudipati & Allamandola 2003; Woon & Park 2004). The plots of neutral anthracene loss and CO_2 growth as a function of photolysis time for different Anth:H_2O concentrations shown in Figure 10 confirm this picture. At all concentrations, CO_2 growth is similar. It rises steadily and continuously with photolysis time. In contrast, PAH loss behavior depends strongly on concentration. After roughly 30 minutes of photolysis, neutral anthracene loss levels off at a value that is determined by concentration. At the highest concentration (Anth:H_2O = 1:20), only about 10% of the neutral anthracene is depleted whereas at the lowest concentration (Anth:H_2O = 1:770), essentially all the neutral anthracene is gone. As shown in earlier work, rapid conversion to the PAH cation accompanies, and mirrors, the initial phase of neutral PAH loss. Thereafter, the PAH cation signal drops (Gudipati & Allamandola 2003; Gudipati 2004, Bouwman et al. 2010, 2011a, 2011b), presumably as the final alcohols, ketones and quinones form.

5. ASTROPHYSICAL IMPLICATIONS

Over the past 30 yr, IR spectroscopic observations made with airborne and orbiting IR telescopes have provided great insight into, and a vast literature on, the ice and dust in dense molecular clouds and star forming regions (e.g., Keane et al. 2001; Gibb & Whittet 2002; Schutte & Khanna 2003; Boogert et al. 2008; van Dishoeck 2004; Öberg et al. 2011 and references
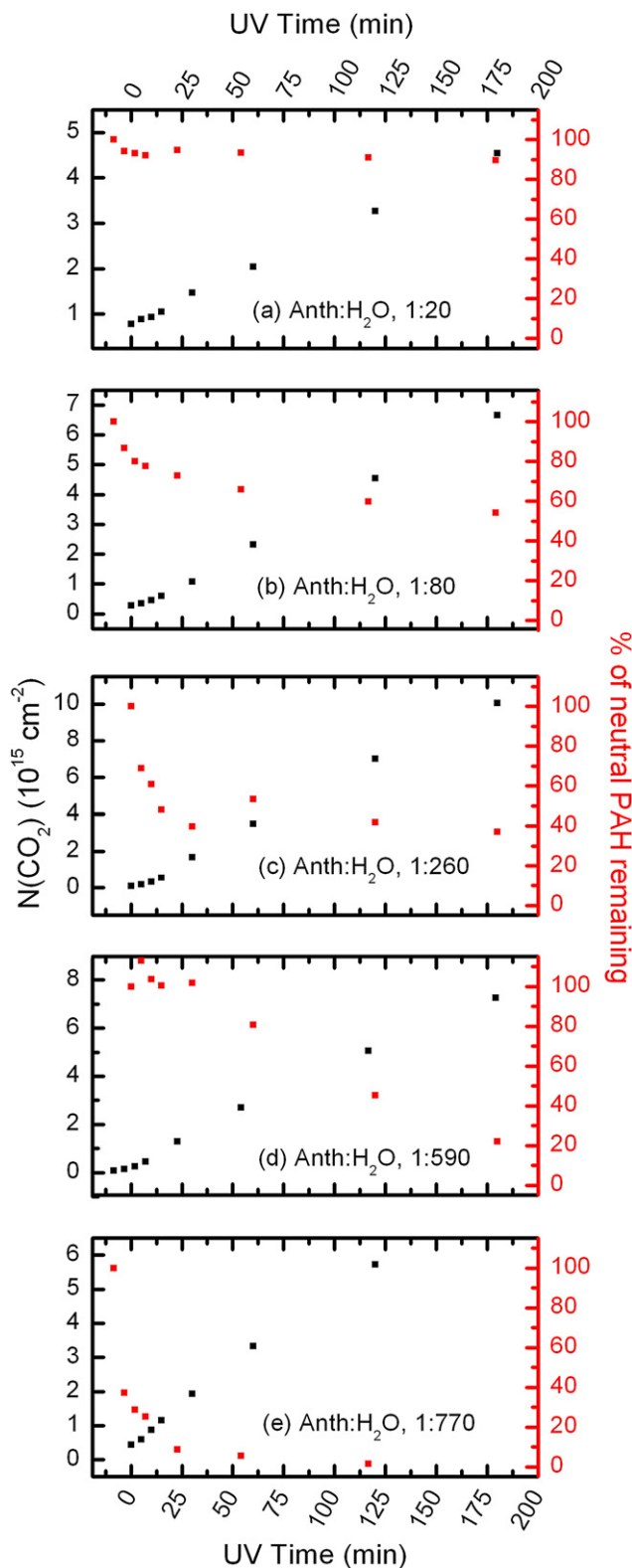
Figure 10. Neutral anthracene loss (red squares) and CO_2 growth (black squares) as a function of VUV irradiation time for the Anth:H_2O ices studied here. Note the contrast between the strong concentration dependence for neutral PAH loss and the slight concentration dependence for CO_2 growth.

therein). Spectra in the 5–9 μm region have been critical to this progress because atmospheric absorptions, combined with strong interstellar ice and dust features, obscure much of the 2.5–3.5 and 9–13 μm regions that are accessible via ground-based telescopes.

Apart from the well-known, moderately strong 6.0 and 6.8 μm bands, the 5–9 μm spectra of dense clouds present many weak to moderately strong features that vary along different lines of sight (e.g., Schutte et al. 1996; Keane et al. 2001; Gibb & Whittet 2002; Schutte & Khanna 2003; Boogert et al. 2008; Öberg et al. 2011 and references therein). Keane et al. (2001), Gibb & Whittet (2002) and Boogert et al. 2008 showed that the 6.0 μm band can be accounted for by the H–O–H bend in water ice blended with an important residual contribution. The residual is comprised of two broad, weak features, one centered near 5.83 μm (1715 cm^{-1}, FWHH between 30 and 50 cm^{-1}), the other centered near 6.3 μm (1590 cm^{-1}, FWHM between 30 and 60 cm^{-1}; Keane et al. 2001). The 6.8 μm feature appears to consist of at least two broad and varying components, one centered about 6.75 μm (1480 cm^{-1}) and one near 6.95 μm (1440 cm^{-1}) (Keane et al. 2001; Schutte & Khanna 2003). In addition to these features between 5.5 and 7 μm, there are also several weak bands between 7 and 8 μm, roughly falling at 7.25, 7.4, 7.58, and 7.68 μm (Schutte et al. 1996; Boogert et al. 1996). In-depth, thorough discussions of these features and their assignments are given by Keane et al. (2001), Schutte & Khanna (2003), Boogert et al. (2008), and Öberg et al. (2011).

In an elegant analysis of 5–8 μm interstellar ice spectra associated with 41 low luminosity Young Stellar Objects (YSOs) measured by *Spitzer*, Boogert et al. (2008) removed the contribution of the broad 6 μm H_2O–ice feature and showed that the residual absorption consists of at least five independent spectroscopic components, with most showing weak but significant substructure. Boogert et al. (2008) present an in-depth, extensive discussion and review of the possible carriers of these components, providing an excellent portal into the literature. They also conclude that all the phenomena observed for ices toward massive YSOs are observed toward low mass YSOs as well, indicating ices in dense clouds and star forming regions have much in common. The five spectroscopic components identified by Boogert et al. (2008), labeled C1 through C5, are shown in Figure 11.

In parallel with the extensive observing programs, equally intense experimental programs dedicated to preparing and studying interstellar ice analogs have been carried out at laboratories around the world. These observational and experimental studies are the foundation of our understanding of interstellar ice composition, chemistry, processes, and physical properties. However, although PAHs are now considered to be widespread and abundant throughout the interstellar medium, few laboratory studies have been carried out on PAH-containing, H_2O-rich ices and, of these, only a handful have studied the IR spectroscopic and chemical changes induced by UV irradiation. To increase our understanding in this area, in Section 5.1 we expand on the studies reported earlier by Bouwman et al. (2011b) with the additional insight provided by the computational spectra presented in Section 3.1 of different photoproducts and, in Section 5.2, by the different photochemical pathways described in Section 4.

5.1. UV Irradiated PAH/H_2O–ice Mixtures and the 5–9 μm Spectra of Dense Molecular Clouds

Figure 11 shows the five spectroscopic, residual interstellar ice features identified by Boogert et al. (2008) that fall between 5.3 and 7.8 μm. For comparison, the panel above contains a composite made up of all the computed aromatic parent and photoproduct bands between 6.1 and 9.7 μm reproduced from the equivalent panels in Figure 4 and listed in Tables 1–3. The computed bands do not extend below 5.8 μm down to 5.3 μm
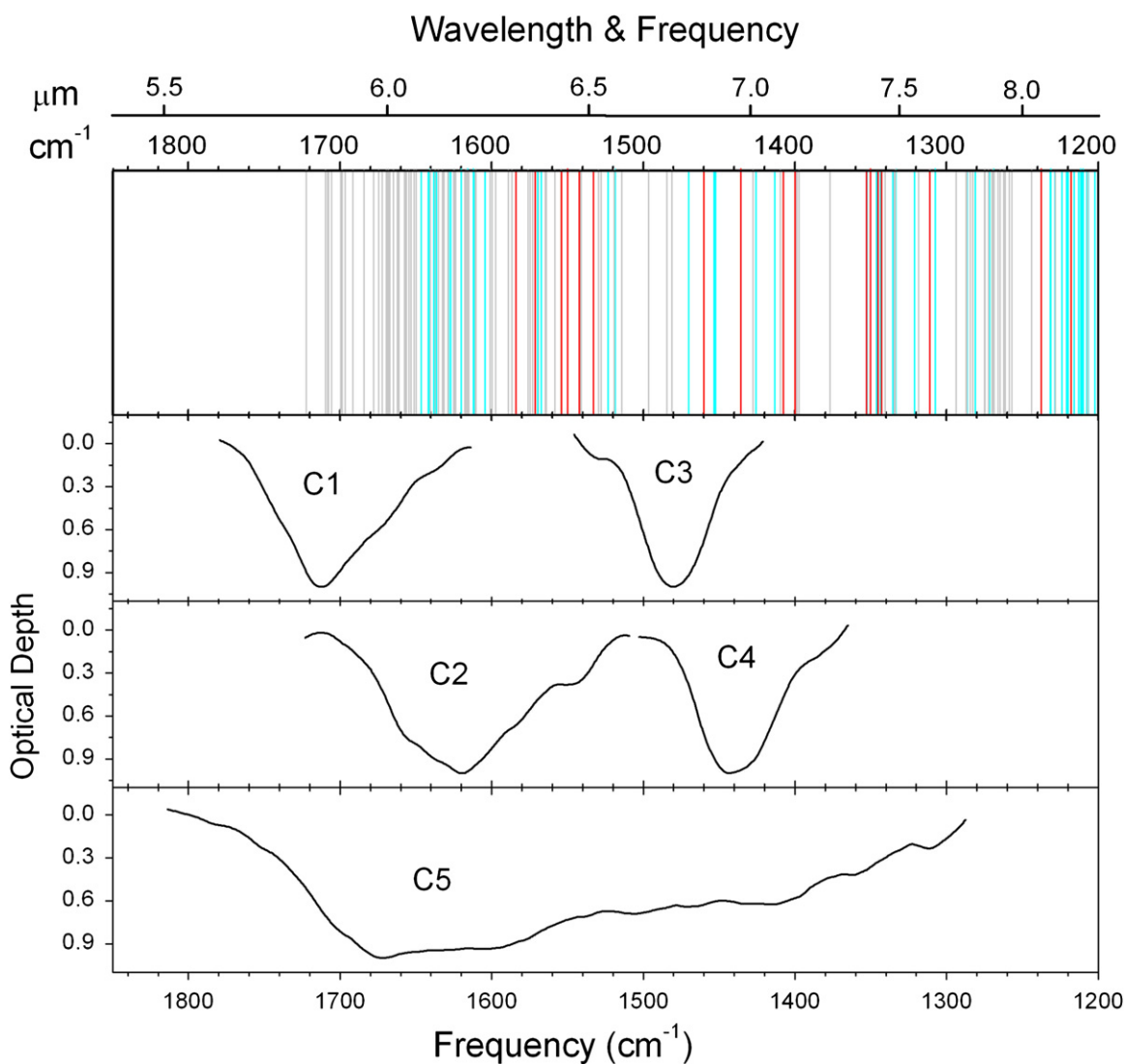
Figure 11. Lower three panels show the C1 through C5 components described by Boogert et al. (2008). These individual components were derived by subtracting the 6.0 μm H_2O feature from spectra of embedded young stellar objects. The top panel corresponds directly to the upper panels shown in Figure 4, in this case showing a superposition of the DFT computed photoproduct bands from all three PAHs studied in this work. Vertical red, cyan, and gray lines correspond to cation bands, PAH-derived alcohols, and PAH-derived ketones/quinones, respectively.

because of limitations in computing the C=O stretch in the ketone forms at the B3LYP/6–31G* level of theory. On the other hand, the spectra of the interstellar residual components do not extend beyond 7.8 μm, presumably due to severe overlap with the blue wing of the 10 μm silicate feature.

Although the size and number of PAHs considered here are small, Figure 11 clearly suggests that the spectra of PAHs and their photoproducts in water-rich ices should be considered as possible contributors to the components described by Boogert et al. (2008). This possibility is now examined, starting at the 5.5 μm end of the spectral window. Throughout this discussion, it is assumed that band broadening and blending from a mixture of ice-bound PAHs and their photoproducts would produce broad, slightly structured features.

Components C1, C2, and the strongest section of C5, span the 5.5–6.5 μm region and extend beyond the panel of computational bands. Bands on the blue half of this region fall in the region characteristic of the very strong C=O stretch in carbonyls. Indeed, C1 is reasonably well accounted for by overlapping C=O stretching bands of well-established, simple interstellar ice species such as HCOOH and H_2CO (see references in Boogert

et al. 2008). While the computational spectra presented here do not extend fully across the C=O stretching region because of the uncertainty inherent the level of theory used, in their study of PAH photochemistry in H_2O ice Guennoun et al. (2011a, 2011b) computed the spectra for the several alcohol and ketone forms of pyrene and coronene photoproducts at the higher, B3LYP/6–3111++g(d, p) level of theory. For these molecules, the C=O stretch falls between roughly 5.5 and 6.25 μm (1740 and 1600 cm^{-1}) and, as with other carbonyls, the C=O stretching bands are by far the strongest (see also Bellamy 1958 and Silverstein & Bassler 1963). Thus, both the relative strength of blue end of the C5 component and its wavelength range are consistent with a strong contribution from aromatic ketones and quinones. While C2 may have some contribution from the C=O stretch in aromatic ketones and quinones, it is distinct from C5 and is centered at the position of the very strong PAH cation CC stretch (Bauschlicher et al. 2010; Boersma et al. 2014), and thus most likely associated with PAH cations.

Keane et al. (2001) attribute excess absorption centered near 6.3 μm (the C2 component from Boogert et al. 2008) in their collection of dense cloud spectra to the aromatic CC stretch and

consider several possible carriers including PAHs in the gas, PAHs condensed on grains, and carbonaceous dust. However, at that time, it was not known that charged PAHs could be present in ices. Attributing the 6.3 μm excess absorption to PAHs in the gas phase, Keane et al. estimated the amount of carbon tied up in PAHs. However, since the intrinsic strength of this band is very sensitive to the degree of ionization, they made two estimates, one based on the intrinsic strength of neutral PAHs, the other for PAH cations. Adopting the intrinsic strength for PAH cations, they calculated that the fraction of elemental carbon tied up in PAHs to be about 7% for NGC 7538:IRS9, an amount consistent with that determined from the PAH IR emission bands. However, assuming neutral PAHs produce the band requires 83% of the elemental carbon. Clearly, this supports the picture that ionized PAHs are components of interstellar ice.

Components C3, C4 and the moderately strong section of C5 span the 6.5–7.8 μm region. Comparing all of these components with the lines in the panel shows they fall in the region of the overlapping, weaker bands associated with aromatic alcohols and ketones, as well as with a smaller number of strong PAH cation bands. The careful work of Keane et al. (2001) and Schutte & Khanna (2003) showed that the 6.8 μm feature is made up of at least two components, one centered near 6.75 μm, the other at 6.95 μm. These are components C3 and C4 identified by Boogert et al. (2008). The computational spectra in Figure 11 show that, while aromatic alcohols and ketones have bands that could contribute to C3, they are sparse and weak, perhaps a fourth the density of the bands near 6.3 μm. On the other hand, this position is associated with aliphatic CH deformation modes and every H_n-PAH will have moderately strong bands here. As with all aliphatic containing materials, these could well contribute to this band. The situation with C4 is similar to that of C3. C4 spans a wavelength region in which aliphatic CH deformation bands are moderately strong. The limited PAH data set in Figure 11 shows that strong PAH cation bands might also contribute to C4. Moving to longer wavelengths, several broad, weak features near 7.24, 7.41, 7.58, and 7.68 μm have been known in the spectra associated with deeply embedded protostars for some time (e.g., Lacy et al. 1991; Schutte et al. 1996; Boogert et al. 1996; Keane et al. 2001) and these all contribute to the 6.5–7.8 μm portion of C5. Figure 11 shows that even this simple mixture of small, pure PAHs, PAH cations, aromatic alcohols and ketones produces a very rich spectrum between 6.5 and 7.8 μm. Together with the property that these bands are intrinsically weaker than the CC PAH cation and C = O stretching bands indicates that PAHs could be important contributors to C5.

5.2. PAH/H_2O-ice Photochemistry, Photoproducts and Astrochemistry

The presence of aromatic alcohols, ketones, ethers and H_n-PAHs in the residues that remained after UV irradiated PAH:H_2O ices were warmed to room temperature is well established (Bernstein et al. 1999; Ashbourn et al. 2007). However, until quite recently, it was not at all clear if these species formed in the low temperature ice during irradiation or afterward, during warm-up, when reactive species could diffuse through the ice. Therefore, while they might be important interstellar ice constituents, significantly influencing astrochemistry and IR observations as discussed in Section 5.1 above, they may only play a role in regions where irradiated ices can warm to well above 100 K. This question is now settled thanks to the novel two-color, laser-desorption,

laser-ionization-TOF experiments by Gudipati & Yang (2012) and Yang & Gudipati (2014). They have shown that the addition of OH and O are the primary chemical reactions that occur in PAH:H_2O ices subjected to Lyα radiation at 5 K. This contrasts with the efficiency of hydrogenation which, they find, is higher at 100 K than at 5 K. Consider also the knowledge summarized in Section 4.1 that PAH cation formation is the first step upon exposure to UV radiation and that aromatic alcohols, ketones and quinones are *also* formed in low temperature PAH:H_2O ices irradiated with near-UV radiation (Guennoun et al. 2011a, 2011b). Taken together, the overwhelming implication is that, in regions where they are subjected to UV radiation, interstellar ices contain PAHs, PAH cations, PAH(-OH)$_n$, and PAH(=O)$_n$ in addition to molecules such as CO_2, CH_3OH, NH_3, etc.

UV-driven PAH erosion, ultimately producing CO, CO_2, and H_2CO from the carbon atoms making up the aromatic network is also important. Although PAHs are likely present at only the few percent level in ice grain mantles and the amount of CO_2 and H_2CO formed via these pathways is small in comparison to the amount formed by grain surface and radiation driven bulk reactions (e.g., Öberg et al. 2010; Fuchs et al. 2009), UV-driven PAH erosion processes in water-rich interstellar ices may help resolve the apparent "contradiction" that the PAHs dominating the IR emitting population are thought to be very large, ($50 < C_n < 100$) whereas, up to now, the PAHs extracted from meteorites are much smaller.

Recent studies have shown the key importance of H_2O in similar UV-driven PAH loss and CO_2 growth. Radich et al. (2014) have shown that, in aqueous media, UV-generated OH radicals trigger graphene (very large PAHs) scission into smaller, PAH-like compounds that, with continued irradiation, produce CO_2 and H_2O. Likewise, Mattioda et al. (2012), who studied PAH photochemistry in different environmental cells, show that the loss of the PAH isoviolanthrene ($C_{34}H_{18}$) with growth of CO_2 occurs only water vapor is present in the chamber.

The UV-driven processes and PAH:H_2O ice chemistry considered here may well be important not only in high radiation field environments, but wherever interstellar ices are found. Interstellar ices experience the low level UV radiation field present throughout dense clouds, based on cosmic ray H ionization and recombination rates. Ices in the vicinity of star and planet forming regions will be exposed to high radiation fields, and ices in protoplanetary disks, formed around the mid-plane, will be brought to the UV-rich outer edges and back to the mid-plane by vertical mixing (e.g., Bouwman et al. 2011b; Öberg et al. 2011, 2013 and references therein). Recently, by modeling an ice particle's movement throughout the disk, Ciesla & Sandford (2012) have shown that the total UV fluences received by the ices in the solar nebula could be considerably greater than experienced by typical ices in dense molecular clouds.

The impact of the work reported here is significant. Foremost among these results is that, in addition to the mixture of species such as H_2O, CH_3OH, NH_3, CO, etc., typical interstellar ices should also contain neutral and ionized PAHs, aromatic alcohols, ketones and quinones. Based on models of PAH freeze-out timescales and different interstellar radiation fields, Bouwman et al. (2011b) estimated that PAHs and PAH photoproducts may comprise 2%–3% of interstellar ice mantles. Their presence within the ice will influence band positions and profiles through structural alterations and complex formation. For example, since some of the CO_2 in an ice mantle may have been produced via the PAH erosion process, its vibrational bands are likely to be perturbed by the adjacent aromatic moiety, affecting band

profile analyses (e.g., Cook et al. 2011). PAHs and their photoproducts will also participate in the chemistry that occurs within the ice and ultimately in the gas as the ices sublime. Similarly, these processes should occur in many other low-temperature, water-rich icy objects in the solar system because aromatics are delivered to the surfaces of most solar system objects in significant quantities by meteorites and interplanetary dust particles (IDPs; Zenobi et al. 1989; Clemett et al. 1993).

6. CONCLUSION

IR spectroscopic studies of vacuum ultraviolet (UV) irradiated anthracene:H_2O, pyrene:H_2O, and benzo[ghi]perylene:H_2O ices (12 K) at various concentrations are reported. Using DFT computed IR spectra to follow the UV driven spectroscopic changes shows that the corresponding parent PAH cations, as well as specific mono- and di-aromatic alcohols [PAH(OH)$_n$] and quinones [PAH(O)$_n$] form. Little evidence is found for hydrogenation at these temperatures, consistent with the findings of Gudipati & Yang (2012).

PAH concentration in the water–ice matrix influences the stability of the PAHs, their photoproducts and the rates and efficiencies of photoproduct production. PAH erosion is tracked via the final photoproducts, CO_2 and H_2CO. For these small PAHs, PAH erosion and fragmentation is significant, but not as important as PAH(OH)$_n$ and PAH(O)$_n$ formation. PAHs are likely present at only the few percent level in ice grain mantles, and the amount of CO_2 and H_2CO formed via these pathways is small in comparison to the amount formed by grain surface and radiation driven bulk reactions (e.g., Öberg et al. 2010; Fuchs et al. 2009). However, UV-driven PAH erosion processes in water-rich interstellar ices may help resolve the apparent "contradiction" that the PAHs dominating the IR emitting population are thought to be very large, ($50 < C_n < 100$) whereas, up to now, the PAHs extracted from meteorites are much smaller. Formation of PAH-related photoproducts is most efficient at low PAH concentrations; this is consistent with a higher concentration of monomers, as opposed to PAH aggregates. Monomers react more readily with H and OH radicals than PAH aggregates. As PAH concentration drops below PAH:$H_2O \sim$ 1:300, PAH ionization and stabilization becomes increasingly important and PAH cations determine the dominant photochemical pathways followed in PAH:H_2O ices.

DFT computed spectra are used to assess the contribution of PAH-related species to the interstellar ice absorption features between 5 and 9 μm. PAH cations are important contributors to the C2 component and PAH(OH)$_n$ and PAH(O)$_n$ to the C5 component described by Boogert et al. (2008). Thus, apart from simple species such as CO, CO_2, CH_3OH, NH_3, etc., typical interstellar ices should also contain neutral and ionized PAHs, aromatic alcohols, ketones, and quinones at the few percent level with respect to H_2O.

PAHs, their photoproducts, and ion-mediated processes should therefore be considered when modeling interstellar ice processes, spectroscopy and astrochemistry. PAHs and PAH-related processes should also be important for water-rich icy objects in the solar system.

REFERENCES

Allamandola, L. J., Hudgins, D. M., & Sandford, S. A. 1999, ApJL, 511, L119
Allamandola, L. J., Sandford, S. A., & Tielens, A. G. G. M. 1992, ApJ, 399, 134
Allamandola, L. J., Sandford, S. A., & Valero, G. J. 1988, Icar, 76, 225
Ashbourn, S. F. M., Elsila, J. E., Dworkin, J. P., et al. 2007, M&PS, 42, 2035
Bauschlicher, C. W., Jr., Boersma, C., Ricca, A., et al. 2010, ApJS, 189, 341
Bauschlicher, C. W., & Langhoff, S. R. 1997, AcSpA, 53, 1225
Bauschlicher, C. W., & Ricca, A. 2010, MoPh, 108, 2647
Becke, A. D. 1993, JCP, 98, 5648
Bellamy, L. J. 1958, The Infra-Red Spectra of Complex Molecules (London: Methuen & Co. Ltd.)
Bernstein, M. P., Mattioda, A. L., Sandford, S. A., & Hudgins, D. M. 2005a, ApJ, 626, 909
Bernstein, M. P., Moore, M. H., Elsila, J. E., et al. 2003, ApJL, 582, L25
Bernstein, M. P., Sandford, S. A., & Allamandola, L. J. 2005b, ApJS, 161, 53
Bernstein, M. P., Sandford, S. A., & Allamandola, L. J. 1996, ApJL, 472, L127
Bernstein, M. P., Sandford, S. A., Allamandola, L. J., et al. 1999, Sci, 283, 1135
Bernstein, M. P., Sandford, S. A., Mattioda, A. L., & Allamandola, L. J. 2007, ApJ, 664, 1264
Boersma, C., Bauschlicher, C. W., Jr., Ricca, A., et al. 2014, ApJS, 211, 8
Boogert, A. C. A., Schutte, W. A., Tielens, A. G. G. M., et al. 1996, A&A, 315, L377
Boogert, A., Pontoppidan, K., Knez, C., et al. 2008, ApJ, 678, 985
Bouwman, J., Cuppen, H. M., Bakker, A., Allamandola, L. J., & Linnartz, H. 2010, A&A, 511, A33
Bouwman, J., Cuppen, H. M., Steglich, M., Allamandola, L. J., & Linnartz, H. 2011a, A&A, 529, A426
Bouwman, J., Mattioda, A. L., Linnartz, H., & Allamandola, L. J. 2011b, A&A, 525, A93
Bregman, J. D., Hayward, T. L., & Sloan, G. C. 2000, ApJL, 544, L75
Brooke, T. Y., Sellgren, K., & Geballe, T. R. 1999, ApJ, 517, 883
Ciesla, F. J., & Sandford, S. A. 2012, Sci, 336, 452
Chang, Q., & Herbst, E. 2014, ApJ, 787, 135
Chiar, J. E., Tielens, A. G. G. M., Whittet, D. C. B., et al. 2000, ApJ, 537, 749
Clemett, S. J., Maechling, C. R., Zare, R. N., Swan, P. D., & Walker, R. M. 1993, LPSC, 24, 309
Cook, A. M., Mattioda, A. L., Quinn, R. C., et al. 2014, ApJS, 210, 15
Cook, A. M., Whittet, D. C. B., Shenoy, S. S., et al. 2011, ApJ, 730, 124
Cuylle, S. H., Allamandola, L. J., & Linnartz, H. 2014, A&A, 562, A22
Dauben, W. G., Salem, L., & Turro, N. J. 1975, AcChR, 8, 41
d'Hendecourt, L. B., Allamandola, L. J., Grim, R. J. A., & Greenberg, J. M. 1986, A&A, 158, 119
Flükiger, P., Lüthi, H. P., Portmann, S., & Weber, J. 2000, MOLEKEL 4.2 (Swiss Center for Scientific Computing: Manno, Switzerland)
Frisch, M. J., Pople, J. A., & Binkley, J. S. 1984, JCP, 80, 3265
Frisch, M. J., et al. 2009, Gaussian 09, Revision C.01 (Wallingford, CT: Gaussian, Inc.)
Fuchs, G. W., Cuppen, H. M., Ioppolo, S., et al. 2009, A&A, 505, 629
Garozzo, M., La Rosa, L., Kanuchova, Z., et al. 2011, A&A, 528, A118
Gerakines, P. A., & Moore, M. H. 2001, Icar, 154, 372
Gibb, E. L., & Whittet, D. C. B. 2002, ApJL, 566, L113
Giuliano, B. M., Reva, I., Lapinski, L., & Fausto, R. 2012, JCP, 136, 024505
Gudipati, M. S. 2004, JPCA, 108, 4412
Gudipati, M. S., & Allamandola, L. J. 2003, ApJL, 596, L195
Gudipati, M. S., & Allamandola, L. J. 2006, ApJ, 638, 286
Gudipati, M. S., & Yang, R. 2012, ApJL, 756, L24
Guennoun, Z., Aupetit, C., & Mascetti, J. 2011a, PCCP, 13, 7340
Guennoun, Z., Aupetit, C., & Mascetti, J. 2011b, JPCA, 115, 1844
Hardegree-Ullman, E. E., Gudipati, M. S., Boogert, A. C. A., et al. 2014, ApJ, 784, 172
Hudgins, D. M., Bauschlicher, C. W., & Allamandola, L. J. 2005, ApJ, 632, 316
Hudgins, D. M., Sandford, S. A., & Allamandola, L. J. 1994, JPhCh, 98, 4243
Hudgins, D. M., Sandford, S. A., Allamandola, L. J., & Tielens, A. G. G. M. 1993, ApJS, 86, 713
Keane, J. V., Tielens, A. G. G. M., Boogert, A. C. A., Schutte, W. A., & Whittet, D. C. B. 2001, A&A, 376, 254
Keheyan, Y., & ten Kate, I. L. 2012, Orig. Life Evol. Biosph., 42, 179
Lacy, J. H., Carr, J. S., Evans, N. J., II, et al. 1991, ApJ, 376, 556
Langhoff, S. R. 1996, JPhCh, 100, 2819

Mattioda, A. L., Cook, A. M., Ehrenfreund, P., et al. 2012, AsBio, 12, 841
Mattioda, A. L., Hudgins, D. M., & Allamandola, L. J. 2005, ApJ, 629, 1188
Mattioda, A. L., Hudgins, D. M., Bauschlicher, C. W., Rosi, M., & Allamandola, L. J. 2003, JPCA, 107, 1486
Michalska, D., Bienko, D. C., Abkowicz-Bienko, A. J., & Latajka, Z. 1996, JPC, 100, 17786
Noble, J. A., Dulieu, F., Congiu, E., & Fraser, H. J. 2011, ApJ, 735, 121
Oba, Y., Watanabe, N., Kouchi, A., Hama, T., & Pirronello, V. 2010, ApJL, 712, L174
Öberg, K. I., Boamah, M. D., Fayolle, E. F., et al. 2013, ApJ, 771, 95
Öberg, K. I., Boogert, A. C. A., Pontoppidan, K. M., et al. 2011, ApJ, 740, 109
Öberg, K. I., van Dishoek, E. F., Linnartz, H., & Andersson, S. 2010, ApJ, 718, 832
Peeters, E., Allamandola, L. J., Hudgins, D. M., Hony, S., & Tielens, A. G. G. M. 2004, in ASP Conf. Ser. 309, Astrophysics of Dust, ed. A. N. Witt, G. C. Clayton, & B. T. Draine (San Francisco, CA: ASP), 141
Radich, J. G., Krenselewski, A., Zhu, J., & Kamat, P. V. 2014, Chem. Mater., 26, 4662
Ricca, A., & Bauschlicher, C. W. 2000, CPL, 328, 396
Roser, J. E., Ricca, A., & Allamandola, L. J. 2014, ApJ, 783, 97

Sandford, S. A., Bernstein, M. P., & Allamandola, L. J. 2004, ApJ, 607, 346
Sandford, S. A., Bernstein, M. P., & Materese, C. K. 2013, ApJS, 205, 8
Schutte, W. A., Allamandola, L. J., & Sandford, S. A. 1993, Icar, 104, 118
Schutte, W. A., & Khanna, R. K. 2003, A&AS, 298, 1049
Schutte, W. A., Tielens, A. G. G. M., Whittet, D. C. B., et al. 1996, A&A, 315, L333
Sellgren, K., Brooke, T. Y., Smith, R. G., & Geballe, T. R. 1995, ApJL, 449, L69
Silverstein, R. M., & Bassler, G. C. 1963, Spectrometric Identification of Organic Compounds (New York: Wiley)
Smith, R. G., Sellgren, K., & Tokunaga, A. T. 1989, ApJ, 344, 413
Stephens, P. J., Devlin, F. J., Chabalowski, C. F., & Frisch, M. J. 1994, JPhCh, 98, 11623
Tielens, A. G. G. M. 2008, ARA&A, 46, 289
van der Zwet, G. P., Allamandola, L. J., Baas, F., & Greenberg, J. M. 1985, A&A, 145, 262
van Dishoeck, E. F. 2004, ARA&A, 42, 119
Warneck, P. 1962, ApOpt, 1, 721
Watanabe, M., & Kouchi, A. 2002, ApJ, 567, 651
Woon, D. E., & Park, J. 2004, ApJ, 607, 342
Yang, R., & Gudipati, M. S. 2014, JCP, 140, 104202
Zenobi, R., Philippoz, J. M., Buseck, P. R., & Zare, R. N. 1989, Sci, 246, 1026